Distributed Hydrologic Modeling in Northwest Mexico Reveals the Links between Runoff Mechanisms and Evapotranspiration

AGUSTÍN ROBLES-MORUA

School of Earth and Space Exploration, Arizona State University, Tempe, Arizona

ENRIQUE R. VIVONI

School of Earth and Space Exploration, and School of Sustainable Engineering and the Built Environment, Arizona State University, Tempe, Arizona

ALEX S. MAYER

Department of Civil and Environmental Engineering, Michigan Technological University, Houghton, Michigan

(Manuscript received 31 August 2011, in final form 30 January 2012)

ABSTRACT

A distributed hydrologic model is used to evaluate how runoff mechanisms—including infiltration excess (R_I), saturation excess (R_S), and groundwater exfiltration (R_G)—influence the generation of streamflow and evapotranspiration (ET) in a mountainous region under the influence of the North American monsoon (NAM). The study site, the upper Sonora River basin (~9350 km^2) in Mexico, is characterized by a wide range of terrain, soil, and ecosystem conditions obtained from best available data sources. Three meteorological scenarios are compared to explore the impact of spatial and temporal variations of meteorological characteristics on land surface processes and to identify the value of North American Land Data Assimilation System (NLDAS) forcing products in the NAM region. The following scenarios are considered for a 1-yr period: 1) a sparse network of ground-based stations, 2) raw forcing products from NLDAS, and 3) NLDAS products adjusted using available station data. These scenarios are discussed in light of spatial distributions of precipitation, streamflow, and runoff mechanisms during annual, seasonal, and monthly periods. This study identified that the mode of runoff generation impacts seasonal relations between ET and soil moisture in the water-limited region. In addition, ET rates at annual and seasonal scales were related to the runoff mechanism proportions, with an increase in ET when R_S was dominant and a decrease in ET when R_I was more important. The partitioning of runoff mechanisms also helps explain the monthly progression of runoff ratios in these seasonally wet hydrologic systems. Understanding the complex interplay between seasonal responses of runoff mechanisms and evapotranspiration can yield information that is of interest to hydrologists and water managers.

1. Introduction

Arid and semiarid regions of the southwest United States and northwest Mexico are influenced significantly by the North American monsoon (NAM). This atmospheric circulation pattern is responsible for generating a large proportion of the annual rainfall, ranging from 40% to 80% (e.g., Douglas et al. 1993; Vivoni et al. 2008) and up to 85% of the annual streamflow during July, August, and September (Gochis et al. 2006). The in-phase relationship between precipitation and radiation suggests that correspondence may exist between runoff mechanisms, which typically depend on seasonal wetness, and the land–atmosphere interactions arising during the NAM. Several studies have investigated how soil moisture plays a role in land–atmosphere exchanges and their impact on subsequent rainfall generation in the NAM region (e.g., Small 2001; Xu et al. 2004; Vivoni et al. 2009). This interaction arises from a positive soil moisture–rainfall feedback (Eltahir 1998) that has been shown to operate in the region during the summer season, aided by ecosystem greening (e.g., Dominguez et al. 2008;

Corresponding author address: Enrique R. Vivoni, School of Earth and Space Exploration and School of Sustainable Engineering and the Built Environment, Arizona State University, Bateman Physical Sciences Center, F-Wing, 650-A, Tempe, AZ 85287-1404.
E-mail: vivoni@asu.edu

DOI: 10.1175/JHM-D-11-0112.1

Méndez-Barroso and Vivoni 2010). To our knowledge, however, an analysis has not been performed of the relationship between evapotranspiration (ET) and the underlying runoff mechanisms in the NAM region.

Various studies have investigated the partitioning of precipitation into ET and runoff and their relationship with soil moisture using climate models (e.g., Luo et al. 2007; Hamlet et al. 2007). For example, Hamlet et al. (2007) found that trends of ET and runoff ratios in the western United States were strongly linked to the trends in seasonal precipitation. Other studies have related the aridity index to runoff ratios and compared empirical equations to climate model simulations with the purpose of exploring the relationships between ET and runoff (e.g., Arora 2002; Koster and Suarez 1999; Sankarasubramanian and Vogel 2002). Prior analyses, however, have not taken into account the interplay between seasonal responses of runoff mechanisms and evapotranspiration. Given the heterogeneous landscape in the NAM region (e.g., Mascaro and Vivoni 2010), the spatial variability in runoff components and their link to land surface fluxes merits more detailed attention. Therefore, the objective of this study is to explore if a relation exists between seasonal runoff mechanisms and ET within the NAM region.

Prior studies have also addressed streamflow seasonality in the NAM region (Brito-Castillo et al. 2003; Gochis et al. 2006). However, understanding the spatiotemporal variability of streamflow remains an elusive challenge for several reasons. First, most regional river basins, particularly within Mexico, remain ungauged (or poorly gauged) because of inadequate rainfall, weather, and/or streamflow records. Sparse data limit the ability to observe hydrologic variables of interest at the appropriate spatiotemporal scales for streamflow forecasting. Second, the NAM region experiences large temporal variations of meteorological characteristics (Gochis et al. 2007; Gebremichael et al. 2007; Nesbitt et al. 2008) and in ecosystem dynamics (Vivoni et al. 2007b; Forzieri et al. 2011). Meteorological conditions also occur upon a template of high topographic variability (Coblentz and Riitters 2004), which lead to large spatial gradients in landscape conditions that are difficult to capture within streamflow simulations. Finally, the region is characterized by pulsed flood events occurring in a summer season of high wetness concurrent with elevated evapotranspiration demands (Vivoni et al. 2010). These phenomena lead to a complex interplay between event-scale and seasonal responses that have not been captured in prior analyses or forecasts (e.g., Gochis et al. 2006; Muñoz-Arriola et al. 2009).

A few studies have investigated streamflow generation and runoff processes in NAM areas within Mexico (García-Oliva et al. 1995; Gutiérrez and Hernandez 1996; Mora and Iverson 1998; Descroix et al. 2002a,b). Descroix et al. (2007) evaluated the role of soil and vegetation characteristics on infiltration- and saturation-excess runoff mechanisms at four sites in Mexico through a modeling approach and comparisons with field data. The authors found that both runoff mechanisms were scale dependent and decreased with larger catchment areas, which is consistent with work by Goodrich et al. (1997) in Arizona. More importantly, Descroix et al. (2007) argued that specific combinations of vegetation and soil types influenced the partitioning between infiltration- and saturation-excess runoff. Catchments with forests, woody savannas, or grasslands on permeable soils were found to be dominated by saturation-excess runoff, whereas areas with less dense vegetation or pastures on lower conductivity soils exhibited higher infiltration-excess runoff. These field observations indicate that a rich set of runoff mechanisms are possible and that numerical models could be useful for to capturing their spatial organization.

In this study, we use a distributed hydrologic model, the Triangulated Irregular Network (TIN)–based Real-time Integrated Basin Simulator (tRIBS; Ivanov et al. 2004; Vivoni et al. 2007a), to explore the spatial and temporal variability and patterns of streamflow, runoff mechanisms, and evapotranspiration in a large river basin ($\sim$9350 km^2) within the NAM region. Physically based, distributed hydrologic models are tools for generating streamflow predictions that explicitly represent landscape properties and meteorological forcing and their associated spatiotemporal changes (Smith et al. 2004; Wood et al. 2011). Because of the sparse nature of meteorological data in the NAM region, we explored the use of the North American Land Data Assimilation System (NLDAS; Mitchell et al. 2004) as forcing for the spatially distributed model. NLDAS fields were compared, and in some cases adjusted, with ground observations in the study basin prior to the model application, as suggested by Luo et al. (2003) and Pinker et al. (2003). Driving hydrologic models with spatially and temporally variable meteorological fields is considered critical in the NAM region because of the pulsed nature of storm events and the strong gradients in atmospheric conditions imposed by complex terrain (Vivoni et al. 2009).

Through the model application, we pursue the question of whether a link exists between runoff generation and surface fluxes in the heterogeneous landscapes of the study basin. Since the model captures gradients in terrain, soil, vegetation, and aquifer properties, it provides streamflow forecasts that are linked to underlying runoff mechanisms, including infiltration-excess, saturation-excess, and groundwater exfiltration types (Vivoni et al. 2007a). Thus, we determine whether runoff mechanism patterns could be useful for inferring ET

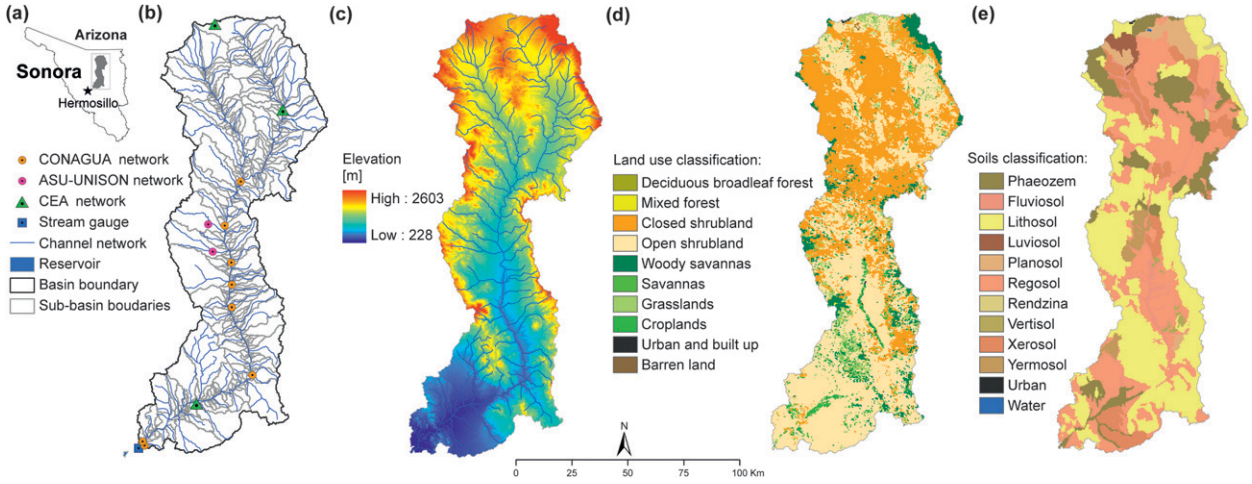

FIG. 1. (a) USR basin location in Sonora, Mexico; (b) subbasin delineation, stream network, and ground station locations; (c) 28-m ASTER elevation distribution; (d) 463-m MODIS vegetation classification; (e) 446-m INEGI–INIFAP soil classification.

(or vice versa). We examine the impact of different meteorological forcings by comparing fields from a sparse network of ground stations, raw products from NLDAS, and the NLDAS products adjusted using available data. These scenarios are evaluated with respect to their impact on the spatiotemporal links between runoff generation and ET. Identifying the value of NLDAS products in the NAM region would have important implications for other river basins with sparse data—in particular within northwest Mexico. Combining modeling frameworks that capture spatially explicit meteorological and watershed conditions is also important to generate useful predictions for water managers and decision makers in the region (e.g., Robles-Morua et al. 2012).

2. Methods

a. Study region

The study site is the upper Sonora River basin (USR), the largest of three subbasins that form the Sonora River, covering 44% of the basin. Figure 1a shows the location of USR basin. The basin has an arid to semiarid climate with a mean annual rainfall from 355 mm near Hermosillo to 711 mm at higher elevations (Hallack-Alegria and Watkins 2007). The headwaters are located near the mining town of Cananea, Sonora, and are shared with the transboundary San Pedro River (e.g., Serrat-Capdevila et al. 2007). The USR flows south until its final destination in the Adolfo Félix Valdez reservoir, which is known as ''El Molinito'' (Fig. 1b). Elevations range from 228 to 2603 m (mean elevation of 1033 m), slopes range from 0° to 69° (mean slope of 10.8°), and aspects are primarily east and west facing (Fig. 1c), as determined from a 28-m digital elevation model (DEM) from the Advanced Spaceborne Thermal Emission and Reflection Radiometer (ASTER). Basin physiographic features include rugged bedrock slopes, dissected foothills and piedmonts, alluvial valleys along the river, and lower-elevation flatlands (INEGI 2000a).

The distribution of vegetation and soils in the region is strongly linked to the complex topography (Coblentz and Riitters 2004; Vivoni et al. 2007b). A 463-m vegetation classification from the Moderate Resolution Imaging Spectroradiometer (MODIS) was used to describe land cover in the basin (Fig. 1d). The dominant vegetation types in the USR basin are open and closed shrublands (85% of the total area) and include desert and subtropical grass, shrub, tree, and succulent species (Vivoni et al. 2007b, 2010). Other important vegetation types include woody savanna and conifer forests at higher elevations and riparian woodlands and croplands. Brown (1994) and Paredes-Aguilar et al. (2000) provide detailed descriptions of the vegetation communities in this region. Soil distributions are known from soil surveys (resampled to 446 m) and include phaeozems, fluviosols, lithosols, luviosols, regosols, xerosols, and yermosols (INEGI–INIFAP 2001; Fig. 1e). Lithosols and regosols occupy 67% of the basin. Lithosols with shallow depths are located in steep hillsides, while regosols are located near alluvial areas but have poor organic contents. According to Descroix et al. (2007), soils in arid and semiarid areas of northern Mexico have characteristics that generally promote infiltration-excess runoff.

The ground observations consist of 13 weather and rain gauge stations from three different networks (Fig. 1b; Table 1): Comisión Estatal del Agua (CEA), Comisión

TABLE 1. Characteristics of the weather station and rain gauge sites in the USR basin available for the study period (1 Jun 2007–31 May 2008), including annual rainfall estimates from three meteorological forcing scenarios. The coordinate system is Universal Transverse Mercator (UTM), zone 12N, 1984 World Geodetic System (WGS84) datum.

ID	UTM easting (m)	UTM northing (m)	Elevation (m)	Network ID	Type	G_i (mm yr^{-1})	Raw P_i (mm yr^{-1})	Adj P_i (mm yr^{-1})
ceacan	568 072	3 427 928	1568	CEA	Weather	720.4	468.6	580.1
ceabac	598 981	3 388 907	1031	CEA	Weather	598.7	420.2	468.2
cnaarz	580 190	3 355 943	807	CONAGUA	Rain	497.3	429.1	451.8
uso139	565 190	3 336 805	739	ASU–UNISON	Rain	403.4	416.1	471.3
cnasqp	575 406	3 335 771	713	CONAGUA	Rain	575.5	416.1	471.3
uso138	567 259	3 324 391	694	ASU–UNISON	Rain	375.2	445.3	461.1
cnaban	577 475	3 318 960	638	CONAGUA	Rain	450.0	445.3	461.1
cnahue	576 052	3 309 133	625	CONAGUA	Rain	474.0	479.4	466.9
cnaach	575 535	3 299 305	606	CONAGUA	Rain	482.8	479.4	466.9
cnamaz	585 363	3 268 787	479	CONAGUA	Rain	657.0	483.7	604.4
ceaure	559 759	3 255 080	369	CEA	Weather	469.9	423.8	542.7
cnatop	535 704	3 238 181	283	CONAGUA	Rain	415.0	369.7	469.1
cnaore	536 245	3 236 191	272	CONAGUA	Rain	416.3	369.7	469.1

Nacional del Agua (CONAGUA), and Arizona State University and Universidad de Sonora (ASU–UNISON). Stations were selected because of their full year of continuous data from 1 June 2007 to 31 May 2008, identified as the period with highest data availability from 2004 to 2008. CEA and ASU–UNISON sites contain hourly rainfall data, with additional weather parameters at CEA stations. CONAGUA sites with daily rainfall observations are used here to improve spatial coverage. Using the daily CONAGUA stations, we determined that the study period had average rainfall as compared to the long-term mean. For example, the average annual rainfall (50 years) at the cnaban station (Table 1) was 444 mm as compared to the 450 mm recorded for the study period.

A manual stream gauging location (''El Oregano'') is located upstream of the El Molinito reservoir. While this site was used to delineate the USR boundary (Fig. 1b), the daily stream discharge measurements at the site are subject to high uncertainties because of the discharge calculation methodology and the impact of several impoundments and diversions upstream of the gauging site. Further, as detailed in the following, the hydrologic model focuses on simulations of the tributary inflows to the main river stem in the USR basin rather than the integrated discharges in the main stem, reducing the need to use the daily flows at the basin outlet.

b. Distributed hydrologic model application

The tRIBS model is a fully distributed model of hydrologic processes (Ivanov et al. 2004; Vivoni et al. 2007a), accounting for 1) canopy interception, 2) evapotranspiration from bare soil and vegetated surfaces, 3) infiltration and soil moisture redistribution, 4) shallow subsurface transport, and 5) overland and channel flow. The rainfall–runoff response is obtained by tracking infiltration fronts, water table fluctuations, and lateral soil moisture fluxes in the vadose and saturated zones. Single infiltration fronts interact with the prestorm moisture profile, determined from hydrostatic equilibrium, and the water table position. This interaction leads to a range of soil moisture states, which influence infiltration and runoff generation. Thus, total runoff (R_T) is composed of four mechanisms resulting from possible model states: infiltration excess (R_I), saturation excess (R_S), groundwater exfiltration (R_G), and perched return (R_P) components as

$$R_T = R_I + R_S + R_G + R_P. \quad (1)$$

Soil moisture states also influence ET, which includes evaporation of canopy water, plant transpiration, and soil evaporation. Individual components are based on the atmospheric demand, derived from energy balance calculations using the Penman–Monteith equation and soil moisture or canopy water availability. Additional model details can be found in Ivanov et al. (2004).

The tRIBS model operates on individual catchments represented by a TIN consisting of elevation, channel, and boundary nodes that capture topographic features and allow a reduction in the number of computational elements (Vivoni et al. 2004). A TIN is associated with a Voronoi polygon network that serves as the finite-volume domain for mass balance and flux calculations. For the USR basin, we selected 291 subbasins draining into the USR main river based on having a Horton–Strahler order greater than 3 at the confluence with the main stem. Figure 1b shows the boundaries for all subbasins, which occupy 92% of the USR basin area, derived from terrain processing of the 28-m ASTER DEM. For each subbasin, we generated a TIN based on the

TABLE 2. Model parameters for major soil types and vegetation classes in the USR basin. The percentages of area of each soil and vegetation class relative to the total USR basin are shown.

			Major soil types (88% of total area)			
			Phaeozem	Lithosol	Regosol	Xerosol
Soil properties	Variable	Units	11.15	36.36	31.70	8.75
Saturated hydraulic conductivity	K_s	(mm h^{-1})	9.24	6.81	25.00	10.57
Soil porosity	n	(—)	0.50	0.49	0.45	0.48
Soil depth	Z_r	(m)	1	1	1	1
Saturated soil moisture content	θ_s	(—)	0.43	0.44	0.41	0.44
Residual soil moisture content	θ_r	(—)	0.06	0.07	0.02	0.07
Pore size distribution index	m	(—)	0.19	0.17	0.85	0.21
Soil heat conductivity	k_s	(J m^{-1} s^{-1} K^{-1})	1.31	1.33	0.20	1.34
Soil heat capacity	C_s	(J m^{-3} K^{-1})	2 363 338	2 399 147	1 610 000	2 417 051
			Major vegetation classes (97% of total area)			
			Closed shrubland	Open shrubland	Woody savannas	Grasslands
Vegetation properties	Variable	Units	37.13	48.91	6.20	4.93
Vegetation fraction	v	(—)	0.6	0.6	0.7	0.4
Albedo	a	(—)	0.16	0.16	0.14	0.18
Vegetation height	h	(m)	6	6	10	1
Vegetation optical transmission	k_t	(—)	0.95	0.95	0.6	0.8
Canopy stomatal resistance	r_s	(s m^{-1})	20	20	125	115

slope criteria method described by Vivoni et al. (2004). This method is based on the topographic relevance of elevation points in describing a domain and was applied to guarantee that 30% or more of the original DEM cells were preserved, as suggested by Vivoni et al. (2005). The subbasins had a mean value of the horizontal point density ($d = n_t/n_g$, where n_t and n_g are the number of TIN and DEM nodes, respectively) of $d = 0.49$ and ranged from $d = 0.31$ to $d = 0.66$.

Individual tRIBS simulations were conducted in a serial fashion on a high-performance computing platform. Since the parallelization capabilities in tRIBS (Vivoni et al. 2011) were not available yet, the large domain was divided into individual subbasins (a similar strategy is followed in the parallel version). For each subbasin model domain, we processed terrain, soil, vegetation, bedrock depth, and initial groundwater distributions to provide distributed model parameters and the boundary and initial conditions. Because of the large number of subbasins, the spatially explicit basin properties were derived for the entire USR basin from either remotely sensed or local data sources and then extracted for each particular subbasin. Vegetation types from MODIS were based on the International Geosphere–Biosphere Programme (IGBP) classification consisting of 17 land cover classes. Soil texture types at a resolution of 1:250 000 from INEGI–INIFAP (2001) were based on the Food and Agriculture Organization (FAO) classification. For each subbasin, vegetation and soil classes were directly mapped to the model domain to populate parameters for individual Voronoi polygons.

The model parameterization was carried out by specifying soil hydraulic and thermal properties, vegetation characteristics, and channel routing parameters. In this work, we guided our model parameterization by the calibration and testing study of Vivoni et al. (2010), where field measurements and numerical modeling results were compared at an eddy covariance tower and in a ~100-km^2 basin located in the Sonora River (outside of the USR). Soil parameter values were based on applying pedotransfer functions (Schapp et al. 2001; Acutis and Donatelli 2003) to the data obtained from the World Soil Database (FAO 1988; Batjes 2002). Vegetation parameters were based on Vivoni et al. (2010) and literature estimates gathered by NLDAS (http://ldas.gsfc.nasa.gov/nldas/) for different ecosystem types. Table 2 lists the parameters used in our study for the major soil and vegetation parameters, including the percentage of basin area occupied by each class. Given the number of subbasin simulations and the lack of hydrologic data in the region, we limited the study to using a consistent set of model parameters derived from prior work and literature values. As shown in Table 2 and Fig. 1, spatial variations in model parameters and their magnitudes are expected to be sufficiently high to induce patterns in the basin response that can lead to different runoff mechanisms within individual subbasins.

Initial and boundary conditions were obtained from studies conducted by CEA. A water table distribution was derived by interpolating manual groundwater depths in wells sampled in 2007. The depth to water table is used in the model as an initial condition for the soil moisture

profile under the assumption of hydrostatic equilibrium (Ivanov et al. 2004). Initial groundwater conditions were allowed to reach dynamic equilibrium by performing a 3-yr continuous spinup period using periodic forcing. This time was determined by performing a series of preliminary simulations using up to 5 years of spinup time. It was found that 3 years of spinup time was sufficient, which is consistent with prior work (Vivoni et al. 2005). We then used a set of electrical soundings and data on aquifer boundaries determined by CEA (2005) to create a distribution of the depth to bedrock in the USR basin. In regions with no aquifer or electrical sounding data, we used a 1-m soil depth determined by Vivoni et al. (2010) from a series of soil profiles. The procedures for deriving the depth to bedrock and initial groundwater level allowed us to capture spatial variations throughout the USR basin that alter the interactions between the unsaturated and saturated zones and lead to different runoff mechanisms.

c. *Numerical experiments and meteorological scenarios*

The modeling experiments in the USR basin consist of three meteorological forcing scenarios (or cases) during a 1-yr simulation. Figure 2 describes the time-varying forcing and spatial inputs used in the modeling scenarios, called GAUGES, NLDAS RAW, and NLDAS ADJ. Time-varying spatial forcings were generated for the period 1 June 2007–31 May 2008 at an hourly resolution. The period was selected to start prior to the NAM season to ensure dry initial conditions that matched the available data from groundwater well records. The period selection also allows for storage changes to undergo an appropriate return to initial conditions during a year and thus could represent an alternative definition for a ''water year'' in the NAM region. This procedure was essential for ensuring that the periodic forcing applied for 3 years yielded a state of dynamic equilibrium in the groundwater system at the end of the spinup.

The GAUGES simulation consists of meteorological forcing to the tRIBS simulations from ground stations, including rainfall (mm h^{-1}), atmospheric pressure (hPa), air temperature (°C), relative humidity (%), and wind speed (m s^{-1}). A Thiessen polygon interpolation was applied to distribute the point-scale measurements. For meteorological data other than rainfall, this implied the use of three weather stations (stations ceacan, ceabac, and ceaure in Table 1). For rainfall, 13 locations provided hourly rainfall data since the CEA and ASU–UNISON networks were augmented with daily CONAGUA rainfall estimates that were downscaled to hourly periods using the hourly fraction of daily rain at the nearest high-resolution gauge.

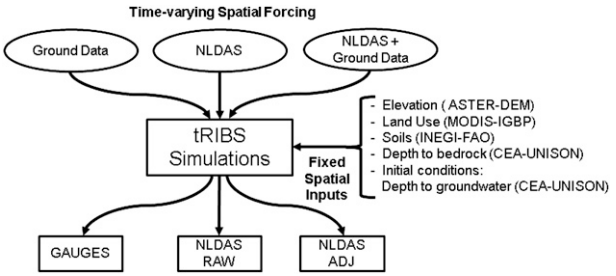

FIG. 2. Schematic representation of three USR simulations (GAUGES, NLDAS RAW, and NLDAS ADJ) resulting from a combination of forcing from ground stations and NLDAS.

Because of the sparse nature of these ground observations, we also evaluated the application of the high-resolution (hourly, 1/8°, or ~12 km) NLDAS forcing, referred to as NLDAS RAW. NLDAS rainfall fields are based on a temporal disaggregation of gauge-only U.S.–Mexico daily analyses (Higgins et al. 2000), adjusted to account for orography using the Parameter-elevation Regressions on Independent Slopes Model (PRISM; Daly et al. 1994). In Mexico, precipitation is temporally downscaled by deriving disaggregated weights from the 8-km Climate Prediction Center morphing technique (CMORPH) hourly data (Joyce et al. 2004). The weather forcing fields of NLDAS were derived from analysis fields of the North American Regional Reanalysis (NARR). The original NARR fields have a 32-km, 3-h resolution and were interpolated to generate the hourly, 1/8° meteorological fields used here (Cosgrove et al. 2003). For the NLDAS RAW scenario, no adjustments were made in the NLDAS fields for the meteorological parameters listed above. An initial comparison of ground rainfall data (from GAUGES) with the corresponding NLDAS pixels resulted in underestimation by NLDAS RAW (see Table 1). Prior validation studies of NLDAS forcing have found similar results, with increased biases at hourly scales (Cosgrove et al. 2003; Luo et al. 2003).

To account for this underestimation, we corrected the NLDAS RAW rainfall by applying the averaged ratio of means (RM) multiplicative factor of Steiner et al. (1999). Bias correction factors were evaluated at hourly and daily scales, with daily factors resulting in a better fit. Here RM was obtained at daily time steps (j) for the study period as

$$\mathrm{RM}(j) = \frac{\sum_{i=1}^{N} g_i(j)}{\sum_{i=1}^{N} p_i(j)}, \tag{2}$$

where N is the number of gauges (i) and corresponding pixels ($N = 13$), and $g_i(j)$ and $p_i(j)$ are daily rainfall

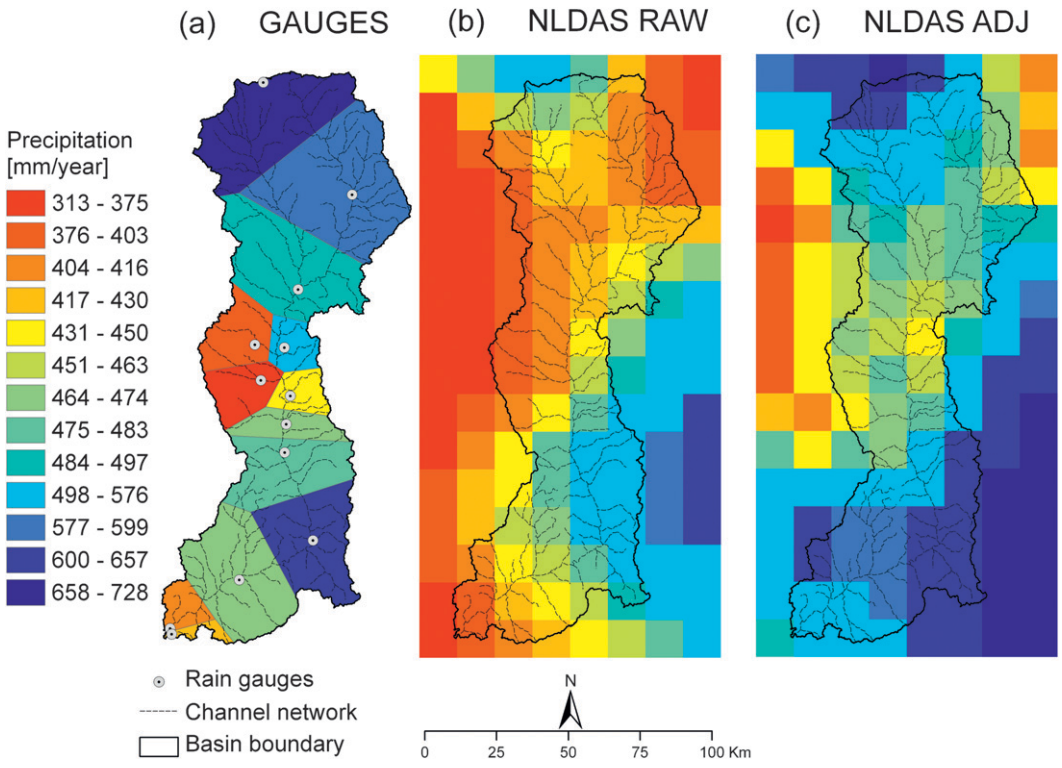

FIG. 3. Spatial variability of annual precipitation for study period for (numbers in parenthesis represent basin-averaged rainfall amounts) (a) GAUGES (542 mm yr^{-1}), (b) NLDAS RAW (430 mm yr^{-1}), and (c) NLDAS ADJ (518 mm yr^{-1}).

values at the gauge and pixel. The mean field bias (B) of Bedient et al. (2008) and the root-mean-square error (RMSE) were used as indicators of the fit. Here B was calculated as

$$B = \frac{1}{N}\sum_{i=1}^{N}\frac{P_i}{G_i}, \tag{3}$$

where G_i and P_i are the total rainfall for the study period. The NLDAS ADJ scenario was derived by applying the daily multiplicative factors, RM(j), to the rainfall data. Table 1 reports the annual precipitation amounts for each station for GAUGES (G_i), NLDAS RAW (Raw P_i), and NLDAS ADJ (Adj P_i). In addition, wind speed from NLDAS RAW overestimated the ground data because of a mismatch between the model outputs at 10-m and the 2-m measurement. Atmospheric pressure was also found to underestimate the ground observations. As a result, we corrected both wind speed and pressure using hourly averaged bias correction factors in a similar fashion as in Eq. (2). It is important to note that the correction factors applied to the NLDAS RAW forcing fields were applied uniformly in the basin. As a result, certain adjustments resulted in the overestimation or underestimation of precipitation, with larger discrepancies in areas located farther away from available stations used to develop the RM factors.

3. Results and discussion

a. Basin-scale variability of rainfall, streamflow, and water balance components

We evaluated the spatially distributed rainfall estimates from the three scenarios for the entire USR basin. Figure 3 shows the annual precipitation of the GAUGES, NLDAS RAW, and NLDAS ADJ for the study period. GAUGES leads to a spatially discontinuous rainfall map because of the Thiessen interpolation and the large variations among stations (Table 1; Fig. 3a). Note the higher rainfall amounts in the northwestern and southeastern areas of the basin. In addition, a distinction exists between drier areas along the central western mountains and wetter areas in the opposing eastern slopes. These general features are also captured in NLDAS RAW, though their spatial extents vary considerably (Fig. 3b). Clearly, the higher resolution of NLDAS fields (~12 km) significantly improves the spatial depiction of rainfall in the USR basin. As shown in Table 1, the corrections to NLDAS resulted in an increase in precipitation for NLDAS ADJ at most locations, while retaining higher spatial variability (Fig. 3c).

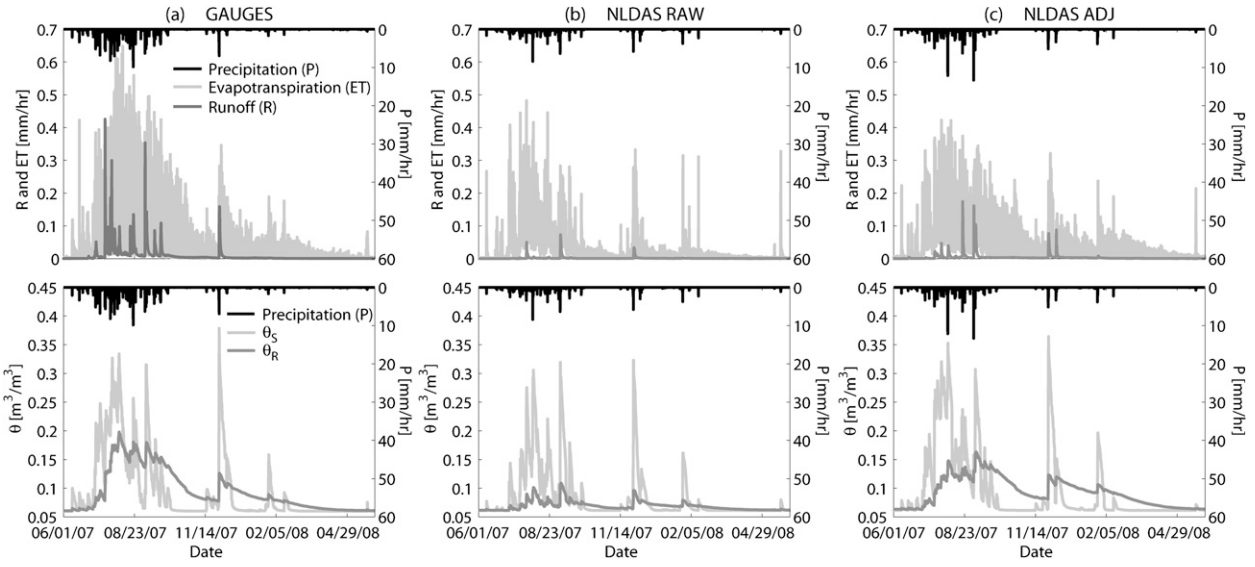

FIG. 4. Simulated basin-averaged precipitation (P, mm h^{-1}), evapotranspiration (ET, mm h^{-1}), runoff (R, mm h^{-1}), soil moisture in top 10 cm (θ_S, m^3 m^{-3}), and soil moisture in the top 1 m (θ_R, m^3 m^{-3}) for (a) GAUGES, (b) NLDAS RAW, and (c) NLDAS ADJ.

Daily spatial adjustments improved the bias between GAUGES and NLDAS ADJ to $B = 0.98$ (from $B = 0.86$ for NLDAS RAW) and reduced the RMSE between collocated sites from 117.9 mm yr^{-1} (NLDAS RAW) to 79.5 mm yr^{-1} (NLDAS ADJ). Further, the basin-averaged rainfall was nearly matched after the adjustment, with GAUGES at 542 mm, NLDAS RAW at 430 mm, and NLDAS ADJ at 518 mm.

Figure 4 presents the basin-averaged temporal dynamics of water balance components for each scenario, including mean areal precipitation (P), evapotranspiration (ET), surface runoff (R), and depth-averaged soil moisture in the 10-cm surface layer (θ_S) and top 1-m root zone (θ_R) at hourly resolution. As expected, temporal variation in the hydrologic system is bimodal with a stronger NAM season (76%–80% of the annual rainfall in July, August, and September) and a weaker winter period. Nevertheless, the time-varying fluxes and states indicate that large differences are present among the three forcing products. The GAUGES scenario exhibits higher P, ET, R, and soil moisture (θ_S and θ_R). We attribute this to the overestimation of rainfall in the northern subbasins due to the sparse sampling by a few stations (Fig. 3). It is interesting to note how differences in P translate to basin-averaged surface runoff, where baseflows are sustained in GAUGES and NLDAS ADJ, but not in NLDAS RAW. In addition, θ_S and θ_R are impacted by differences in precipitation amount and timing. For GAUGES and NLDAS ADJ, a carryover of θ_R is present from summer to winter seasons—an indication that the NAM can set antecedent wetness conditions for fall and winter storm events. This impact is observed in the lower runoff response of NLDAS RAW to a storm event in December. Clearly, the NLDAS RAW scenario has limited runoff and soil moisture dynamics (except in the surface layer) because of the relatively low rainfall. Evapotranspiration is also lower in the NLDAS RAW (ET = 250 mm) case, which is an indication of the stronger soil moisture limitation in relation to the other scenarios (ET = 467 and 417 mm yr^{-1} for GAUGES and NLDAS ADJ). The carryover θ_R also supports ET from plant transpiration during the fall, winter, and early spring in GAUGES and NLDAS ADJ.

The areal-weighted dynamics in the USR basin arise from geographical variations in subbasin characteristics. Figure 5 displays the percent contribution to the total streamflow volume by subbasin. Note that weak correspondence with the total rainfall volume (Fig. 3) is due to the rainfall–runoff transformation. Both rainfall characteristics (intensity, duration, and spatial location) and landscape properties (soil, vegetation, and groundwater depth) influence this transformation. Streamflow in northern regions differed significantly among the scenarios. In northeastern areas, subbasins contributed 16% (GAUGES), 1% (NLDAS RAW), and 2% (NLDAS ADJ) of the total runoff, while northwestern regions contributed higher fractions of total runoff: 25% (GAUGES), 12% (NLDAS RAW), and 21% (NLDAS ADJ). Despite these differences, all scenarios preserved a major feature of the rainfall forcing in that western portions generated more streamflow than eastern ones. This result was caused by lower conductivity (K_S) soils in western subbasins (~10 mm h^{-1}), as compared to eastern areas (~16 mm h^{-1}), and higher slopes in western mountains

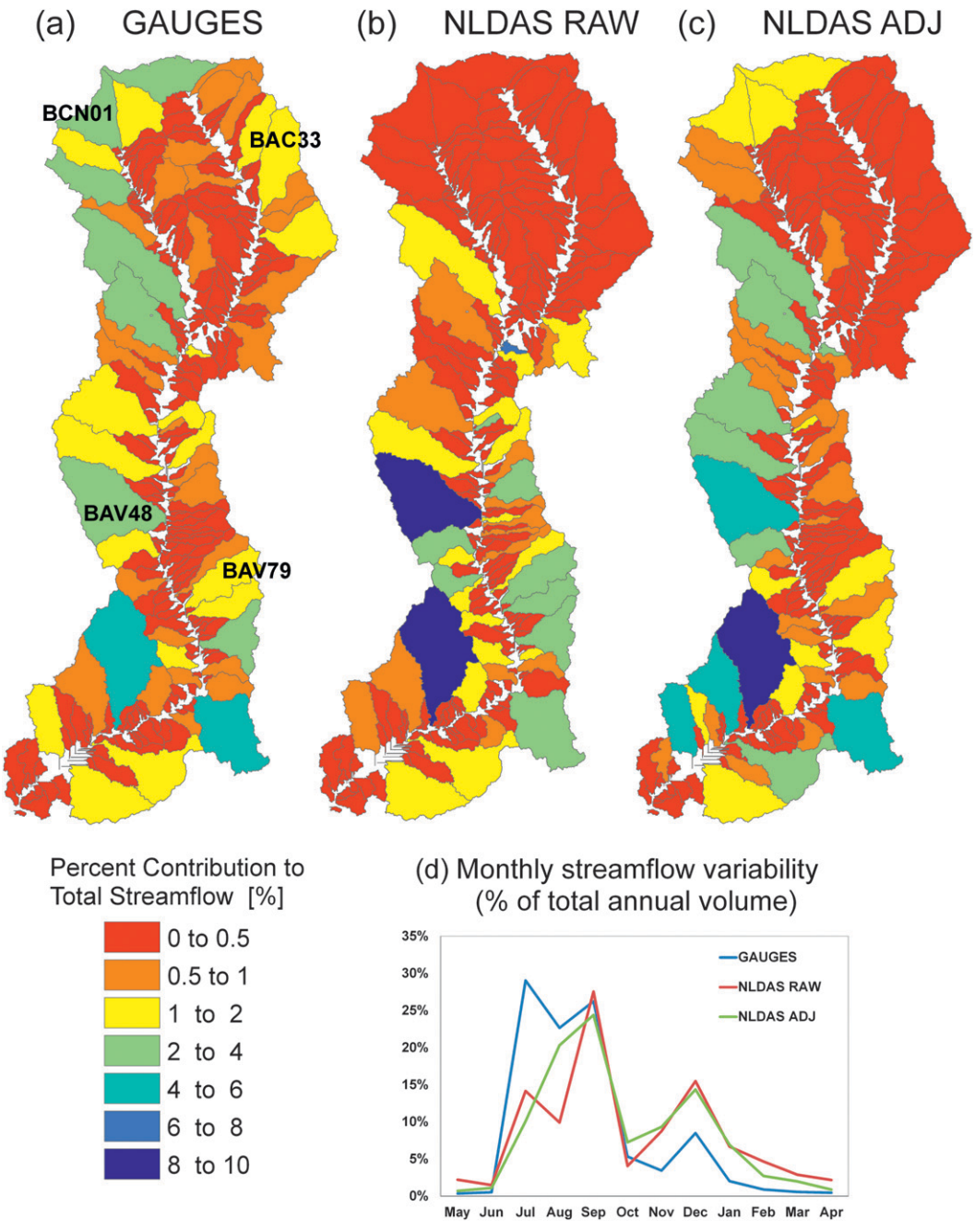

FIG. 5. Spatial distribution of the percent contribution of each subbasin to the total streamflow in the USR basin (numbers in parenthesis represent the total streamflow volumes): (a) GAUGES (574 $Mm^3\ yr^{-1}$), (b) NLDAS RAW (85 $Mm^3\ yr^{-1}$), and (c) NLDAS ADJ (254 $Mm^3\ yr^{-1}$). (d) Monthly streamflow as a percentage of the total annual volume for the three scenarios.

(Fig. 1c). Better agreement among products is found in southern regions because of higher station density. These subbasins contributed the largest percent of total streamflow with 51% (GAUGES), 77% (NLDAS RAW), and 72% (NLDAS ADJ). Figure 5d indicates how the annual volume is distributed during the year. Clearly, rainfall bimodality is translated into two streamflow periods, with higher summer amounts that peak in July (GAUGES) or September (NLDAS RAW and NLDAS ADJ cases) for this year. Note how NLDAS scenarios shift streamflow from summer to winter—an indication that the GAUGES case overestimated rainfall and runoff in summer period

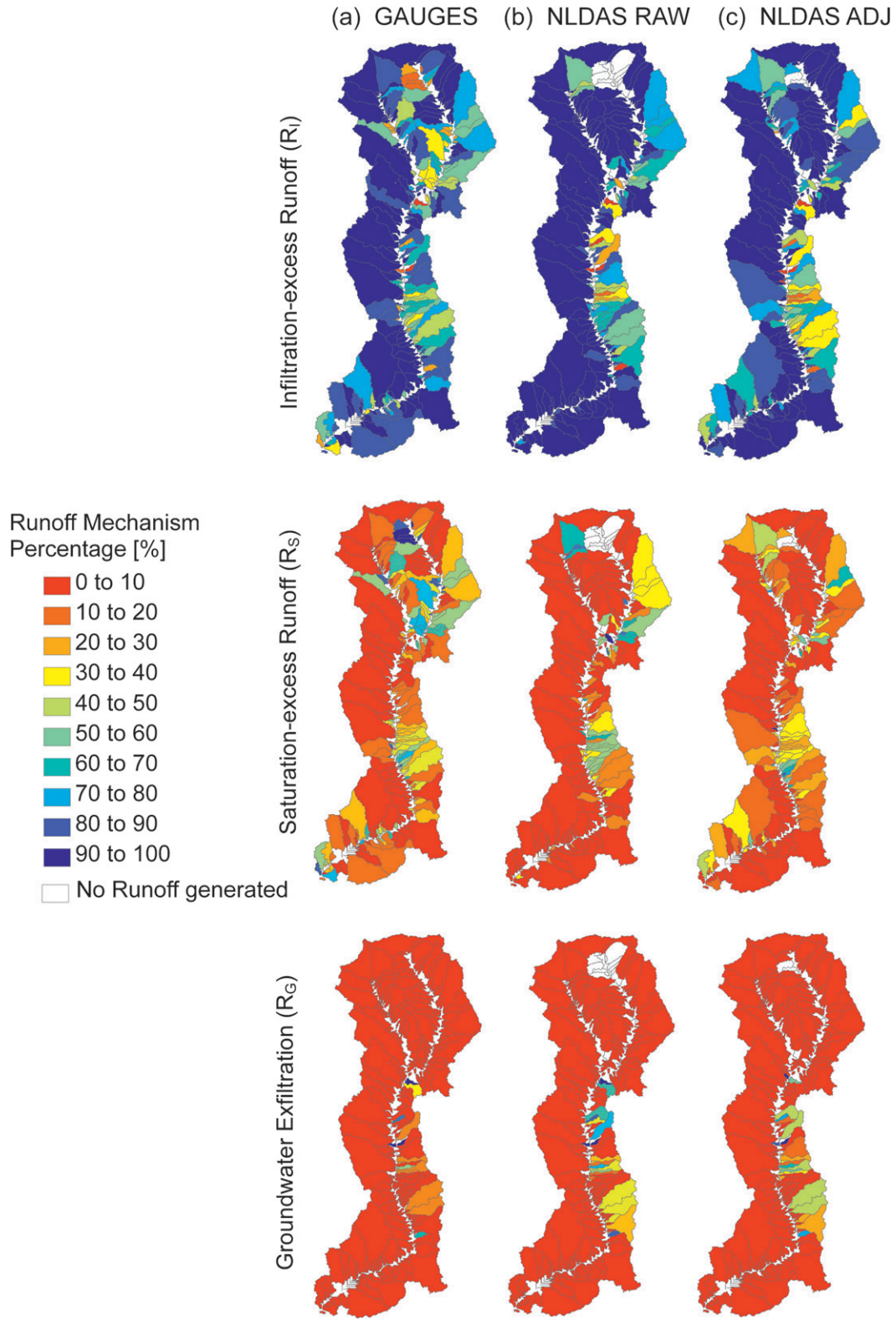

FIG. 6. Spatial distribution of runoff mechanisms as a percentage of total runoff (R_T) for (a) GAUGES, (b) NLDAS RAW, and (c) NLDAS ADJ. (top) Infiltration-excess runoff R_I, (middle) saturation-excess runoff R, and (bottom) groundwater exfiltration R_G.

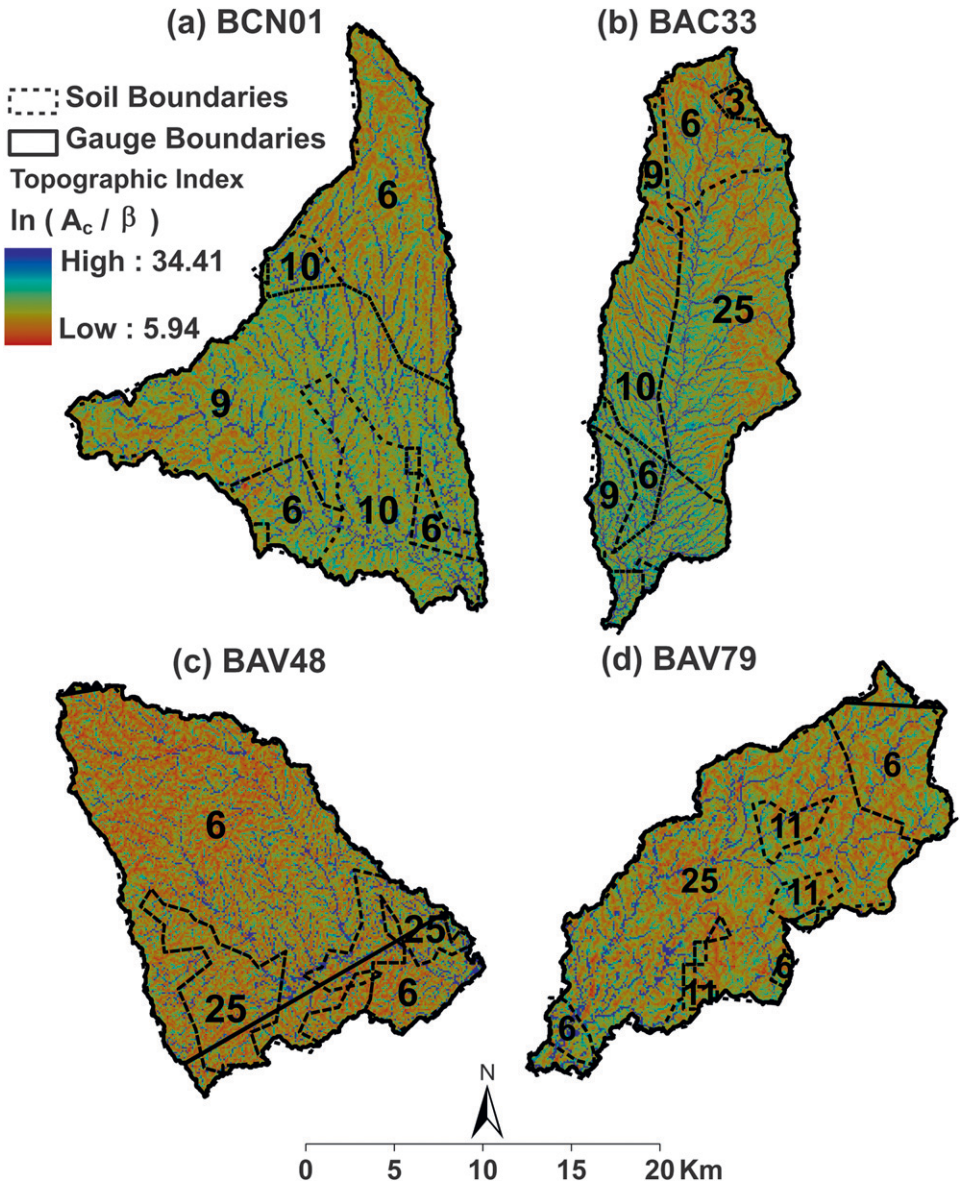

FIG. 7. Topographic index distribution in four selected subbasins: (a) BCN01, (b) BAC33, (c) BAV48, and (d) BAV79. Also shown are boundaries for rain gauge Thiessen polygons and soil map units, where numbers represent the associated value of saturated hydraulic conductivity (K_s, mm h^{-1}).

and underestimated these in the winter. A detailed analysis of the spatial variations of the dominant runoff mechanisms and their relationship to land features is explored in the following section.

b. Runoff generation and underlying mechanisms at the subbasin scale

Spatial distributions in streamflow contributions are related to the underlying runoff mechanisms simulated in the model, as discussed in Vivoni et al. (2007a, 2009). Figure 6 presents the percentage of each major runoff mechanisms in the simulations (R_I, R_S, R_G) relative to the total runoff (R_T) determined at each subbasin outlet. Perched return flow (R_P) was not generated because of the lack of vertical variations in K_S in the model. As expected for arid and semiarid regions with high-intensity rainfall, R_I dominates runoff generation for all scenarios (Fig. 6, top). It is also evident that R_I was more prevalent in western subbasins, where lithosols had lower K_s. Nevertheless, there are subbasins in the northern, eastern, and southern areas with large runoff percentages from R_S. These cases occur on more permeable regosols, where sufficient rainfall input surpasses the soil storage capacity. Interestingly, landscape conditions in eastern

TABLE 3. Characteristics of four selected subbasins (BCN01, BAC33, BAV48, and BAVB79), including terrain, soil, vegetation, rainfall, evapotranspiration, and streamflow properties (see Fig. 5a for locations).

Subbasin properties	BCN01	BAC33	BAV48	BAV79
Area (km^2)	132.15	165.84	292.87	122.10
Mean slope (°)	8.26	9.88	10.97	15.07
Mean elevation (m)	1439.00	1385.16	1021.02	1011.57
Mean λ (–)	11.58	11.73	11.47	11.12
Mean K_s (mm h^{-1})	7.77	15.58	11.43	13.66
Mean n (–)	0.49	0.47	0.48	0.48
Number of rain gauges	1	1	2	2
Number of NLDAS pixels	4	5	6	3
Vegetation cover (% of area):				
Closed shrubland	32%	17%	22%	26%
Open shrubland	55%	57%	58%	42%
Woody savannas	4%	16%	9%	19%
Grasslands	6%	9%	8%	9%
Croplands	3%	1%	3%	4%
Total rainfall (mm yr^{-1})				
GAUGES	720.44	598.71	392.69	482.64
NLDAS RAW	423.36	409.67	416.18	511.38
NLDAS ADJ	558.22	484.09	449.03	548.20
Total ET (mm yr^{-1})				
GAUGES	427.92	526.72	362.55	562.92
NLDAS RAW	201.52	215.57	272.52	333.35
NLDAS ADJ	455.29	373.87	399.61	463.32
Percent contribution to total USR basin streamflow (%)				
GAUGES	2.08	1.93	4.04	1.29
NLDAS RAW	0.14	0.05	8.31	3.56
NLDAS ADJ	1.14	0.08	4.27	1.12

subbasins promoted higher amounts of R_G because of the relatively shallow groundwater depths in this region (Fig. 6, bottom). For example, a total of 15 (GAUGES), 22 (NLDAS RAW), and 23 (NLDAS ADJ) subbasins with total areas of 600, 921, and 997 km^2, respectively, had R_G/R_T of 100%. The underlying physical mechanisms for spatial differences in runoff generation are discussed in the following by selecting four subbasins, labeled in Fig. 5a (BCN01, BAC33, BAV48, and BAV79), that represent the range of spatial variability in runoff generation mechanisms. BCN01, BAC33, BAV48, and BAV79 are naming descriptors used to identify subbasins located in different parts of the USR.

We use the topographic index (λ) of Beven and Kirkby (1979) to classify terrain locations within each subbasin with a similar hydrologic response (Vivoni et al. 2005) and defined as

$$\lambda = \ln\left(\frac{A_c}{\tan\beta}\right), \tag{4}$$

where A_c is the contributing area per unit contour width and β is the local slope angle. Large values of λ indicate areas where runoff is converging and locations that saturate frequently, while lower values of λ represent sites where saturation and runoff do not occur as frequently. Figure 7 shows the spatial distribution of λ for the four subbasins, along with variation of K_s and the boundaries of the rain gauge polygons. To complement these results, Table 3 provides subbasin terrain, soil, and vegetation characteristics for the selected subbasins. Note that vegetation cover is similar across all sites with a large fraction of open and closed shrublands (68%–87% of subbasin areas). In contrast, soil properties, in particular K_s, vary among the subbasins, with a twofold difference in spatially averaged amounts. Subbasin variations in rainfall and landscape properties lead to streamflow contributions ranked in decreasing order as BAV48, BAV79, BCN01, and BAC33, averaged over all scenarios (Table 3).

The runoff mechanisms responsible for streamflow generation in each subbasin are analyzed in Figs. 8 and 9 for the GAUGES and NLDAS ADJ scenarios (results omitted for NLDAS RAW). For each case, the percent of time of occurrence (%) of a runoff mechanism (R_I, R_S, or R_G) is shown as a function of λ. This allows an assessment of the effect of terrain features on runoff production, as well as a measure of the most frequent mechanism. For both scenarios, BCN01 and BAV48 exhibit a dominant contribution of R_I, while BAC33 and BAV79 have more significant periods of R_S and R_G, respectively (also see Fig. 6 for comparison). From these distributions and Fig. 7, we can identify how specific runoff mechanisms are related to subbasin locations and

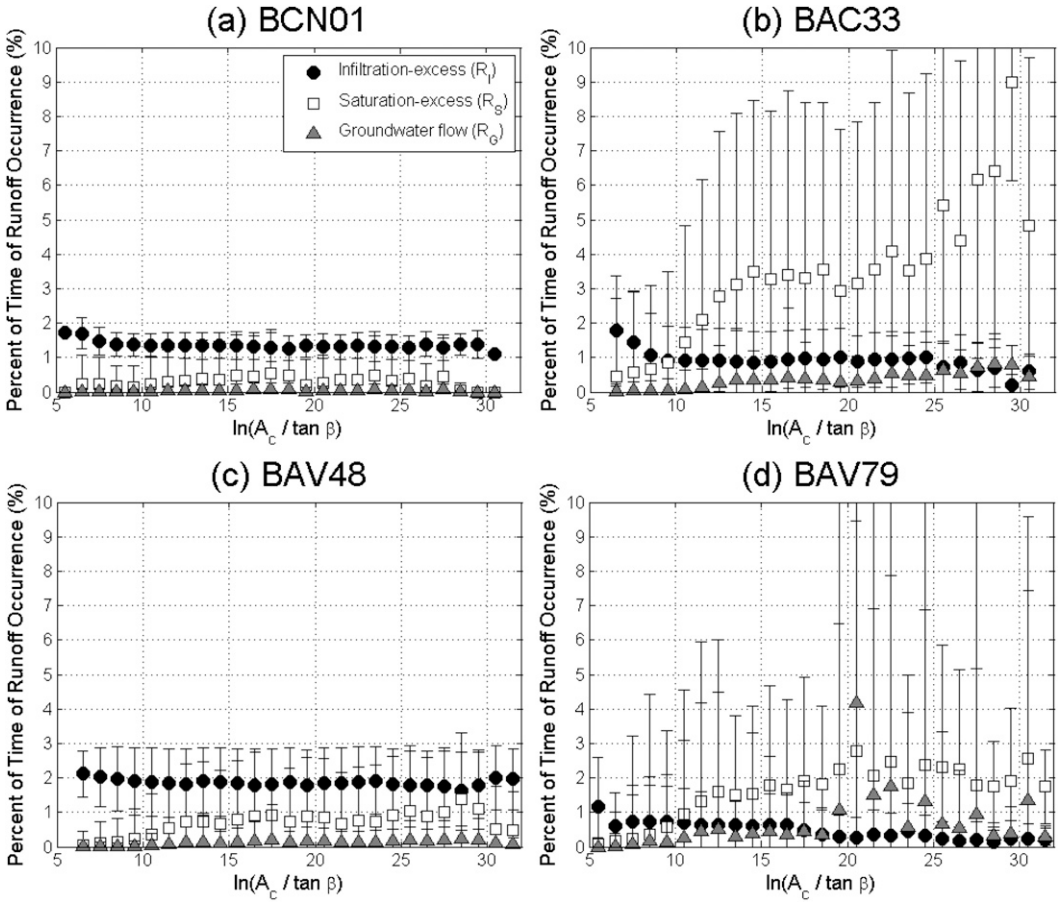

FIG. 8. Runoff mechanism occurrence (percent of total time) variation with the topographic index [$\lambda = \ln(A_c/\tan\beta)$] for four subbasins: (a) BCN01, (b) BAC33, (c) BAV48, and (d) BAV79, in the GAUGES scenario. Vertical bars represent standard deviations of the percent of time of runoff occurrence computed for the corresponding values in the λ bins (bin size = 2 units of λ).

landscape characteristics. For example, subbasin BCN01 is characterized by low K_s, which leads to the dominance of R_I, in particular for GAUGES (Fig. 8a), which had higher rainfall intensities and uniform forcing as compared to NLDAS ADJ (Fig. 9a). Similarly, BAV48 had R_I as a major runoff mechanism because of soils with low K_s, but exhibited higher R_s, especially for regions with higher values of λ located near the channel network. For NLDAS ADJ, R_I and R_S are codominant (Fig. 9c), with R_G contributions in hillslope hollows (intermediate values of λ) and along the main river (high values of λ). In contrast, subbasin BAC33 has higher K_s, which leads to a dominant role for R_S when forced with sufficient rainfall, as in GAUGES (Fig. 8b; 599 mm). A clear increase in R_S with higher λ indicates the role of low-lying floodplain areas in producing runoff (Vivoni et al. 2005). For NLDAS ADJ (Fig. 9b; 410 mm), the low rainfall reduced all runoff occurrences. Interestingly, BAV79 had the most significant R_G under both scenarios, implying less sensitivity to rainfall forcing (Figs. 8d and 9d). As with R_S, groundwater exfiltration increases in frequency within convergent areas (high values of λ), which is an indication that permeable soils and steep slopes sustain a shallow aquifer near the main channel.

Comparisons between these subbasins exemplify the complex interactions between rainfall characteristics (spatial distribution, intensity, and total amount) and landscape properties (soil conductivity, slope, and terrain index) that generate runoff from multiple mechanisms. BCN01 and BAV48 represent northern, western, and southern areas where R_I is the major component and is controlled primarily by low K_s. For these sites, R_S may become codominant under conditions of lower rainfall intensities in NLDAS ADJ, imparting a dependence on terrain features. BAC33, on the other hand, is representative of eastern and northern areas where terrain-mediated R_S is the major component when sufficient rainfall occurs. Under insufficient rainfall amounts,

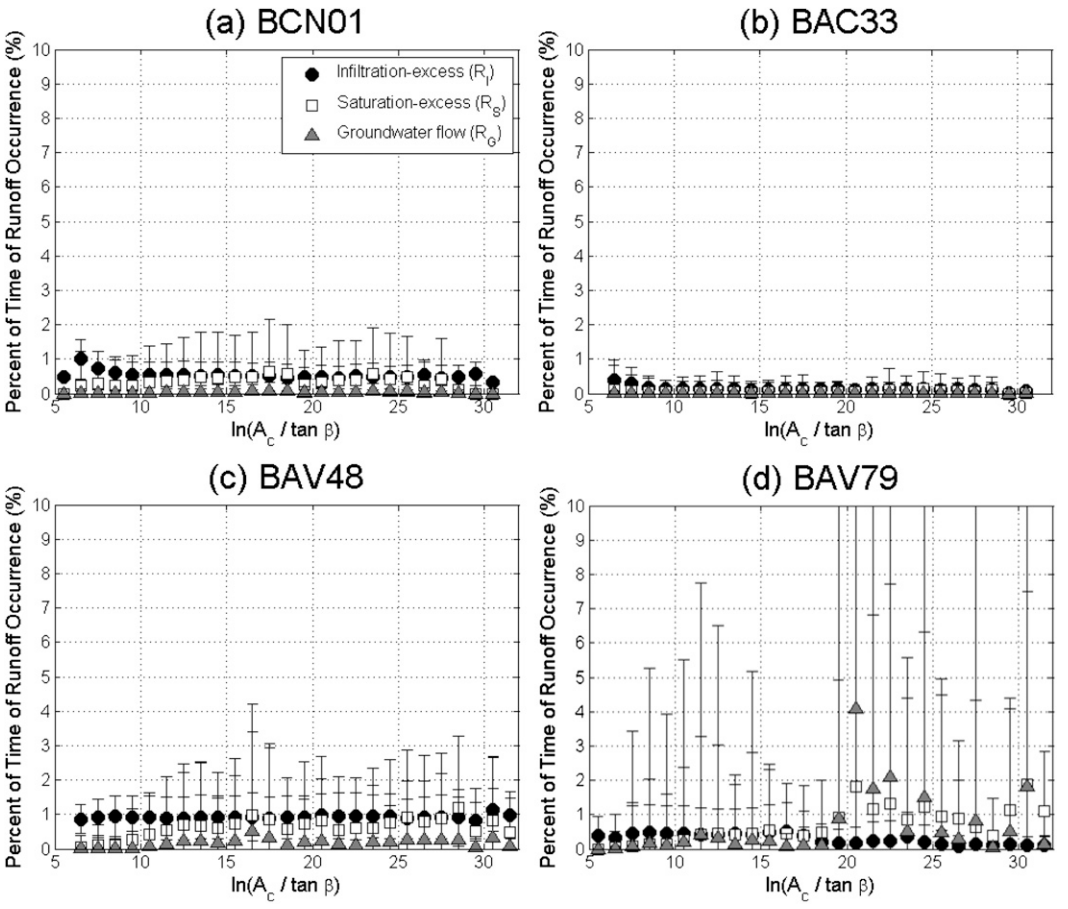

FIG. 9. As in Fig. 8, but for the NLDAS ADJ scenario.

permeable soils in BAC33 reduce runoff for all landscape positions. Finally, BAV79 is a good example of a small set of subbasins in eastern areas that produce R_G consistently and where contributions from R_I and R_S occur under particular rainfall forcings.

c. *Interactions between runoff mechanisms and evapotranspiration*

Spatial variations in the composition of runoff mechanisms should be linked to the land–atmosphere interactions occurring in each subbasin. Figure 10 shows the basin-averaged water balance in the GAUGES and NLDAS ADJ cases, including precipitation (P), evapotranspiration (ET), channel runoff (R), and root zone soil moisture (θ_R). As expected, the subbasin water balance varies considerably from the spatially averaged estimates in the USR basin (Fig. 4). Furthermore, the differences in P, ET, R, and θ_R among individual subbasins are striking, and substantially larger than variations between GAUGES and NLDAS ADJ. Subbasins with R_I as the dominant component (BCN01 and BAV48) exhibit large R pulses of short-duration, more rapid recessions in θ_R and shorter periods of sustained ET. In contrast, in subbasins where R_S and R_G codominate with lower R_I (BAC33 and BAV79), R is sustained over longer periods as baseflow, high θ_R carries over between seasons, and ET is sustained throughout the year. Over the entire period, subbasins with dominant R_I tend to have lower ET/P than those subbasins where R_S and R_G have a significant contribution, as highlighted in Table 3.

To further investigate subbasin differences, we inspect the daily relations between ET and surface soil moisture (θ_S) in Fig. 11. For clarity, these are shown as the piecewise linear regressions of the total ET and daily averaged θ_S obtained at the scale of each subbasin for the GAUGES and NLDAS ADJ scenarios. Piecewise regressions of the ET–θ_S relation are obtained using a nonlinear optimization algorithm (Vivoni et al. 2008) and describe how water limitations in soils influence losses to the atmosphere (Rodríguez-Iturbe and Porporato 2004). For each scenario, a distinction is made between winter [December–February (DJF)] and summer [June–September (JAS)] seasons to capture the variation of the atmospheric demand due to seasonality in radiation. As

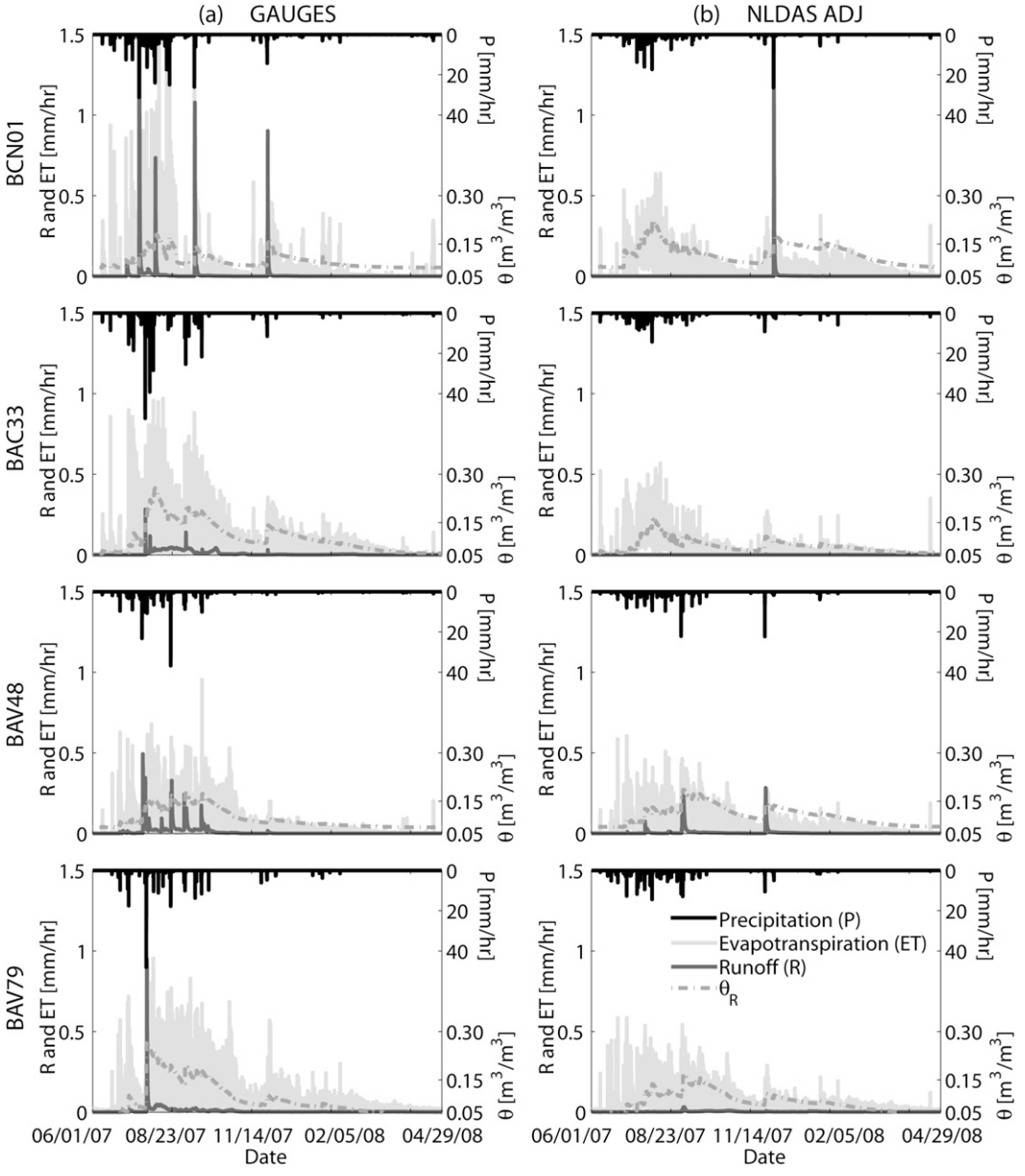

FIG. 10. Water balance components for four subbasins (BCN01, BAC33, BAV48, and BAV79) under (a) GAUGES and (b) NLDAS ADJ scenarios, including precipitation (P, mm h^{-1}), evapotranspiration (ET, mm h^{-1}), runoff (R, mm h^{-1}), and root zone soil moisture (θ_R, m^3 m^{-3}).

expected, daily ET at a given θ_S is higher in JAS. Differences among the subbasins are also more pronounced during the NAM when variations between soil moisture promote maximum ET values ranging from ~4 to 7 mm day^{-1}. Subbasins dominated by R_I (BCN01 and BAV48) have lower ET under dry soil conditions ($\theta_S < 0.1$) in JAS for both scenarios (Figs. 11b,d). This is an indication that infiltration-excess runoff promotes low infiltration, leading to rapid drying in shallow soils, which cannot sustain high ET rates. A clearer distinction of the effect of R_I on the ET–θ_S relation is observed for the GAUGES scenario, likely because of the more frequent runoff production in JAS (Fig. 10). In contrast, subbasins BAC33 and BAV79 with higher R_S and R_G exhibit higher values of ET across all θ_S (GAUGES) and for dry soils (NLDAS ADJ). This result points toward sustained ET even when shallow soils are dry, primarily because of transpiration from the deeper root zone, which remains wet for longer periods because of groundwater contributions. The ET–θ_S relation for subbasins with R_S and R_G

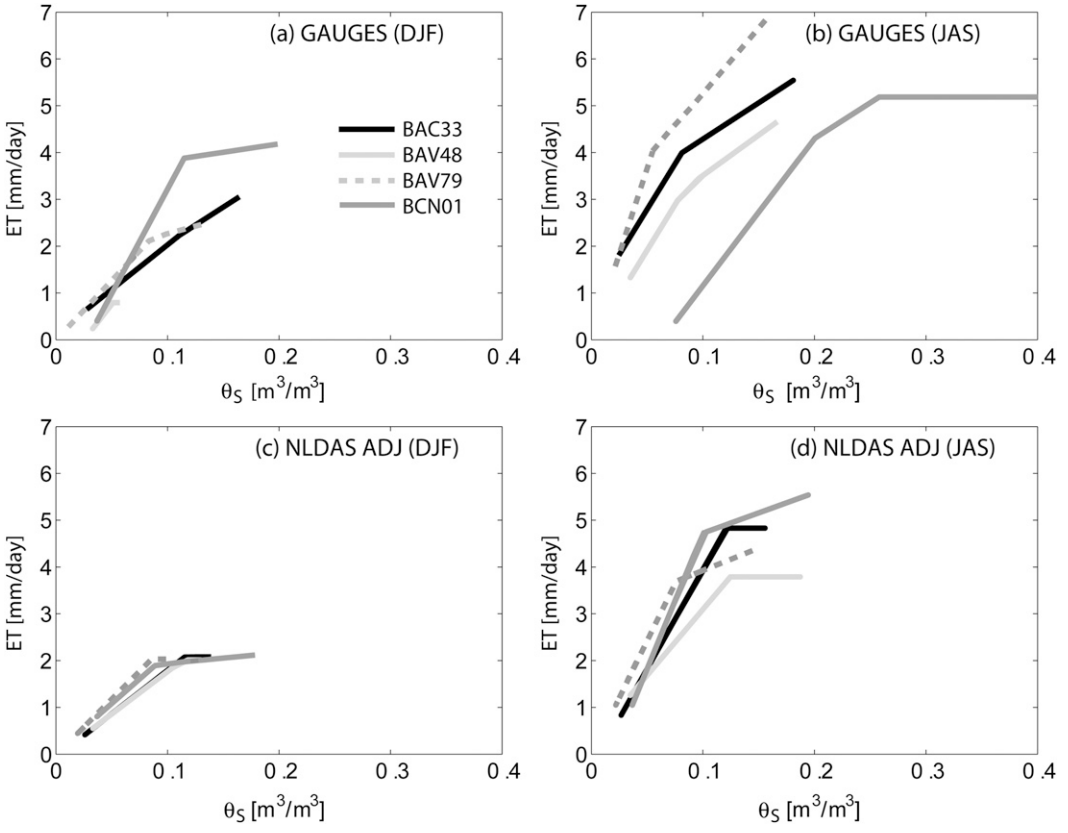

FIG. 11. Daily soil moisture–evapotranspiration relation for (a),(b) GAUGES and (c),(d) NLDAS ADJ scenarios during the (a),(c) winter (DJF) and (b),(d) summer (JAS) months. Total daily ET (mm day^{-1}) and daily averaged surface soil moisture (θ_S) are spatially aggregated in each subbasin (BCN01, BAC33, BAV48, and BAV79). Lines represent piecewise regressions of the daily relationships.

also suggests that ET rates are stressed over shorter soil moisture ranges and reach higher maximum (unstressed) values (also see Vivoni et al. 2008).

We carried out a similar analysis for the entire USR basin to corroborate if the subbasin relations between runoff mechanisms and ET were valid across the region. Figure 12 presents the annual and seasonal ET as a function of the fraction of infiltration-excess (R_I/R_T) and saturation-excess (R_S/R_T) runoff relative to the total runoff (R_T) in all subbasins (291 total). As expected, summer (JAS; bottom row) contributions to the annual ET (top row) are larger than winter (DJF; middle row) values for the GAUGES and NLDAS ADJ cases. A discernible pattern emerges from this analysis. Subbasins with greater R_I/R_T exhibit a decrease in annual ET, whereas subbasins with higher R_S/R_T fractions show an increase in annual ET. While this is clearer in GAUGES, the pattern is also found for the NLDAS RAW (not shown) and NLDAS ADJ scenarios, suggesting that the pattern is robust with regard to the type of rainfall forcing. Subbasins with an increasing R_I/R_T tend to have less infiltration and support lower ET amounts. In contrast, subbasins with increasing R_S/R_T exhibit greater infiltration, which allows higher ET. In addition, subbasins with greater R_S/R_T are also subject to groundwater contributions (Fig. 6) that sustain high soil moisture and ET rates. We evaluated how increases in R_I/R_T were accompanied by decreases in R_S/R_T by estimating the linear correlation (R^2 values) of R_I/R_T versus R_S/R_T for all subbasins. Results show a strong inverse relation for the annual and JAS scales as compared to DJF. In GAUGES, R^2 values for annual and JAS were 0.80 and 0.88, while it is 0.09 for DJF.

Overall, the variations in R_i/R_T can yield annual ET differences of ~400 mm (GAUGES) and ~150 mm (NLDAS ADJ). The seasonal relations also show that the annual trends between ET and runoff mechanisms are consistent for winter and summer. Seasonal patterns, however, are stronger in JAS for GAUGES and in DJF for NLDAS ADJ, which is consistent with the shift in monthly runoff toward winter (Fig. 5d). As a result, NLDAS ADJ summer season exhibits low sensitivity

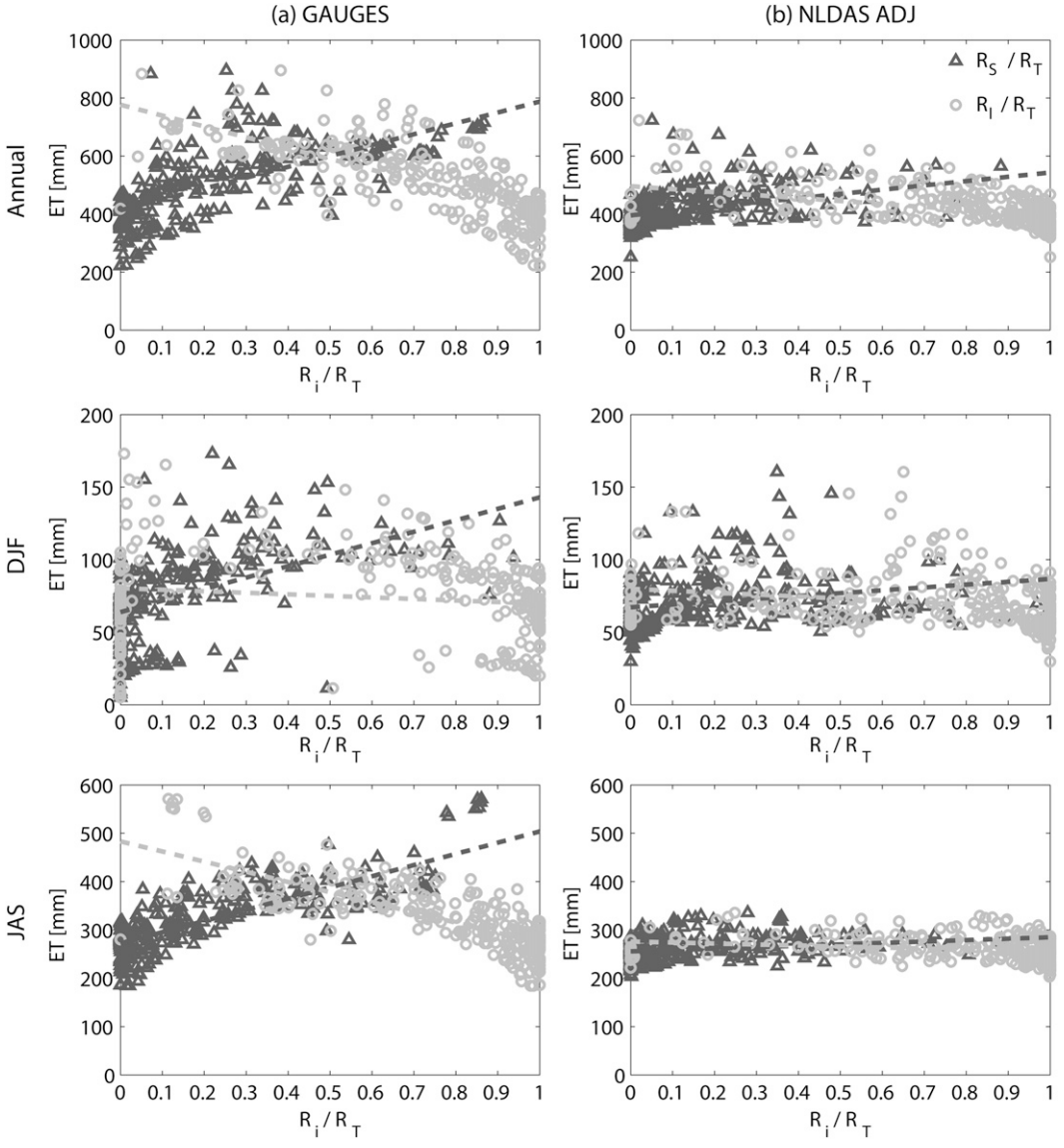

FIG. 12. Annual and seasonal relations between evapotranspiration (ET, mm) and the fraction of infiltration-excess runoff (R_I/R_T) and saturation-excess runoff (R_S/R_T) for (a) GAUGES and (b) NLDAS ADJ. (top) Annual, (middle) winter months (DJF), and (bottom) summer months (JAS). Here R_i represents either R_I or R_S. Dashed lines representing linear regressions between ET and R_i/R_T are included for visualization purposes only.

to the runoff mechanisms. Similarly, we conducted an analysis of the relation of surface soil moisture (θ_S) versus R_I/R_T and R_S/R_T in all subbasins. Increases in R_I/R_T were related to increases in θ_S, while increases in R_S/R_T occurred along with decreases in θ_S. These relations suggest that at the annual and seasonal scale, higher water availability in basins with dominant saturation-excess runoff result in increments of ET that deplete surface soil moisture. Overall, these established links are the outcome of interactions between soil, terrain, and rainfall properties that modulate runoff production and soil moisture for evapotranspiration.

d. Annual and monthly runoff ratios with comparison to empirical estimates

As part of our final analysis, we evaluated the runoff ratios (R/P) at annual, seasonal, and monthly scales to understand the implications of runoff mechanisms and evapotranspiration on streamflow. Figure 13 shows a comparison of runoff mechanism percentages (R_I/R_T, R_S/R_T, and R_G/R_T) during the summer (JAS) for subbasins BCN01 (dominated by R_I) and BAV79 (with significant R_G) in GAUGES and NLDAS ADJ scenarios. The comparisons are limited to summer conditions

when large precipitation events occur. These subbasins were selected because they represent well the range of monthly runoff evolutions across the USR basin. As the NAM progresses from July to September, BCN01 decreases in R_I/R_T and increases in R_S/R_T for both scenarios, whereas the opposite trends are observed in BAV79. Moreover, R_G/R_T contributions in BAV79 increase as the monsoon progresses. This result implies that changes in antecedent wetness (θ_R in Fig. 10), as well as in rainfall intensity, differentially impact the runoff mechanisms in individual subbasins. As a result, we would expect the response in the entire USR basin to be an outcome of individual processes occurring in subbasins with a wide range of landscape properties and meteorological forcing. Table 4 presents monthly runoff mechanism percentages and associated runoff ratio fractions (R_I/P, R_S/P, and R_G/P) for the USR basin, arranged from June 2007 to May 2008 for the different scenarios. Note the higher basin area contributing to runoff (A_R) and the greater proportion of R_I/R_T for the NAM (JAS) relative to other months. In addition, the monthly infiltration-excess runoff ratio increases from $R_I/P = 0.01$–0.02 (June) to $R_I/P = 0.03$–0.16 (September) for the scenarios. An increase in monthly R/P during the NAM is consistent with Gochis et al. (2006) and suggests that infiltration-excess runoff is the major contributor to this process. In contrast, R_S/P and R_G/P play more important roles in the fall and winter seasons.

The spatial variability in annual and seasonal (DJF and JAS) runoff ratios is presented in Fig. 14 for the GAUGES and NLDAS ADJ scenarios. As a reference, we also show the annual runoff ratio (R/P) map in Fig. 14c used by the Mexican government for regional hydrologic studies (INEGI 2000b). The INEGI runoff coefficient estimates are based empirically on the soil permeability, vegetation cover, and the local precipitation intensity, as described in INEGI (2000b). A visual comparison of the annual runoff ratio maps suggests that NLDAS ADJ matches more closely the INEGI (2000b) estimates, which are defined based on a combination of soil and vegetation units (Figs. 1e,d). In particular, areas of low runoff ratio ($R/P < 5\%$) coincide in the northern, eastern, and southern regions. GAUGES, on the other hand, generally overestimates the annual R/P, with certain eastern and western areas having $R/P > 20\%$. As expected, the JAS distributions resemble the annual R/P map since most runoff events occurred in the NAM. In addition, most subbasins during JAS exhibit infiltration-excess runoff ($R_I/R_T > 75\%$; hatched areas) as the dominant mechanism. While R_I/R_T is still a significant contributor to the DJF runoff ratios, certain subbasins with high R_S and R_G (Fig. 6) tend to be responsible for larger winter R/P. In GAUGES and NLDAS ADJ, subbasins with $R/P > 20\%$ are frequent in winter and certain eastern and western subbasins exhibit $R/P > 50\%$ during DJF. These magnitudes are due to baseflow production in subbasins with shallow water tables during the winter, despite the low rainfall amounts. In addition, a large winter rainfall event occurring within certain subbasins with high antecedent wetness carried over from the NAM is also responsible (see Fig. 10).

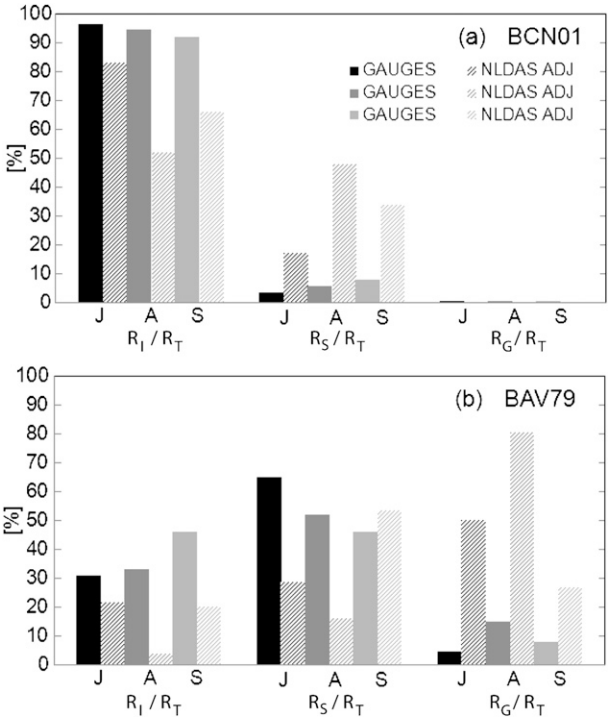

FIG. 13. Percent contribution of runoff mechanisms (R_I/R_T, R_S/R_T, and R_G/R_T) during each summer month (JAS) for GAUGES and NLDAS ADJ in (a) BCN01 and (b) BAV79.

Based on the spatial variations of the annual runoff ratio (R/P), we constructed frequency distributions for the scenarios and compared these to estimates from INEGI (2000b) in Fig. 15. Given the paucity of hydrologic data, INEGI (2000b) represents the best available (and official) runoff estimates valid at the same landscape scale as our simulations. As shown in Fig. 14c, the spatial distribution of INEGI (2000b) corresponds to an intersection of soil and vegetation units with varying runoff potentials. We aggregated these to individual subbasins to compare the simulations to the estimated distribution. While more detailed runoff patterns can be produced by the model (Ivanov et al. 2004), the subbasin representations were considered sufficient for the USR basin. Clearly, GAUGES overestimates the annual R/P because of the misrepresentations in using Thiessen polygons of a set of sparse rain gauges. NLDAS RAW captures well the low R/P in INEGI (2000b) but

TABLE 4. Monthly runoff mechanism percentages (R_I/R_T, R_S/R_T, and R_G/R_T) and monthly runoff ratio fractions (R_I/P, R_S/P, and R_G/P) for the GAUGES, NLDAS RAW, and NLDAS ADJ scenarios. Here A_R is the percentage of the USR basin that is contributing runoff during each month. The monthly runoff ratios are shown as the second row of each month, in italics. Dashed (–) symbols indicate when monthly precipitation was zero and a runoff ratio could not be calculated.

	GAUGES				NLDAS RAW				NLDAS ADJ			
Month	A_R	R_I/R_T	R_S/R_T	R_G/R_T	A_R	R_I/R_T	R_S/R_T	R_G/R_T	A_R	R_I/R_T	R_S/R_T	R_G/R_T
June	74%	80%	9%	10%	34%	65%	6%	29%	34%	66%	9%	25%
	0.02	*0*	*0*		*0.01*	*0*	*0*		*0.01*	*0*	*0.01*	
July	100%	87%	13%	1%	77%	84%	12%	4%	77%	85%	12%	3%
	0.11	*0.02*	*0*		*0.01*	*0*	*0*		*0.02*	*0*	*0*	
August	100%	82%	17%	1%	96%	87%	9%	4%	96%	85%	10%	5%
	0.11	*0.02*	*0*		*0.01*	*0*	*0*		*0.04*	*0*	*0*	
September	100%	85%	14%	1%	82%	88%	10%	2%	82%	78%	20%	2%
	0.16	*0.03*	*0*		*0.03*	*0*	*0*		*0.06*	*0.02*	*0*	
October	85%	75%	14%	11%	56%	77%	6%	16%	56%	60%	11%	29%
	0.80	*0.15*	*0.11*		*0.35*	*0.03*	*0.07*		—	—	—	
November	88%	65%	16%	20%	77%	83%	8%	9%	77%	74%	19%	7%
	0.04	*0.01*	*0.01*		*0.02*	*0*	*0*		*0.05*	*0.01*	*0*	
December	94%	81%	14%	5%	86%	86%	10%	4%	86%	79%	17%	4%
	0.23	*0.04*	*0.01*		*0.10*	*0.01*	*0*		*0.24*	*0.05*	*0.01*	
January	72%	71%	8%	21%	58%	77%	9%	14%	58%	66%	14%	20%
	0.07	*0.01*	*0.02*		*0.04*	*0*	*0.01*		*0.09*	*0.02*	*0.03*	
February	66%	71%	5%	24%	57%	78%	5%	17%	57%	65%	12%	23%
	0.06	*0*	*0.02*		*0.06*	*0*	*0.01*		*0.11*	*0.02*	*0.04*	
March	54%	71%	4%	25%	38%	71%	5%	24%	38%	61%	14%	25%
	0.15	*0.01*	*0.05*		—	—	—		—	—	—	
April	45%	69%	4%	27%	36%	70%	2%	28%	36%	60%	7%	33%
	0.07	*0*	*0.03*		—	—	—		—	—	—	
May	43%	67%	3%	30%	38%	66%	9%	25%	38%	60%	7%	33%
	0.02	*0*	*0.01*		*0.03*	*0*	*0.01*		*0.05*	*0.01*	*0.03*	

underestimates values of $R/P > 5\%$. On the other hand, NLDAS ADJ produces a reasonable match with INEGI (2000b) in particular for $R/P > 5\%$, because of the more realistic rainfall patterns adjusted with ground data. This suggests that adjusted NLDAS products have value as forcing to hydrologic models in remote regions with limited ground observations.

4. Synthesis and conclusions

This study documents an advanced technique for generating hydrologic predictions in mountainous basins under the influence of the NAM, characterized by variable atmospheric conditions. We evaluated the use of meteorological forcing from ground stations and from NLDAS and its adjustment. The scenarios yielded bimodal hydrologic forecasts, with 52%–78% of the annual runoff occurring during the NAM and a secondary winter runoff peak, which is consistent with Gochis et al. (2006) and Brito-Castillo et al. (2003). In addition, the simulations indicated that infiltration-excess runoff was the dominant mechanism, since low conductivity soils cover more than 50% of the area, though both saturation-excess runoff and groundwater exfiltration play important roles in specific regions. These outcomes are in agreement with the observed mixture of runoff mechanisms identified by Descroix et al. (2007). Furthermore, an analysis of the annual runoff ratios from the scenarios resulted in 14% (GAUGES), 3% (NLDAS RAW), and 6% (NLDAS ADJ), which compares well with estimates of 9%–19% from Gochis et al. (2006) and Viramontes and Descroix (2003). Similarly, the runoff ratios during the NAM (14%, 2%, and 4% for GAUGES, NLDAS RAW, and NLDAS ADJ) were consistent with values cited by Gochis et al. (2006) for wetter basins farther south in the region (9%–43%; average of 26%).

The distributed scenarios and hydrologic model afforded the opportunity of quantifying the spatiotemporal features of the watershed response in a large river basin over an annual cycle. Because of limited observations, the characteristics of the basin responses are poorly understood in the NAM region at these spatiotemporal scales (see Vivoni et al. 2009, 2010 for other attempts). We identified how precipitation patterns translated nonlinearly into water balance components, streamflow generation, and runoff mechanisms for a set of subbasins and the entire USR basin. Spatial expressions of different runoff mechanisms were directly related to terrain, soil, and rainfall properties. Analyses in individual subbasins revealed that the prevalence of infiltration-excess runoff depended primarily on

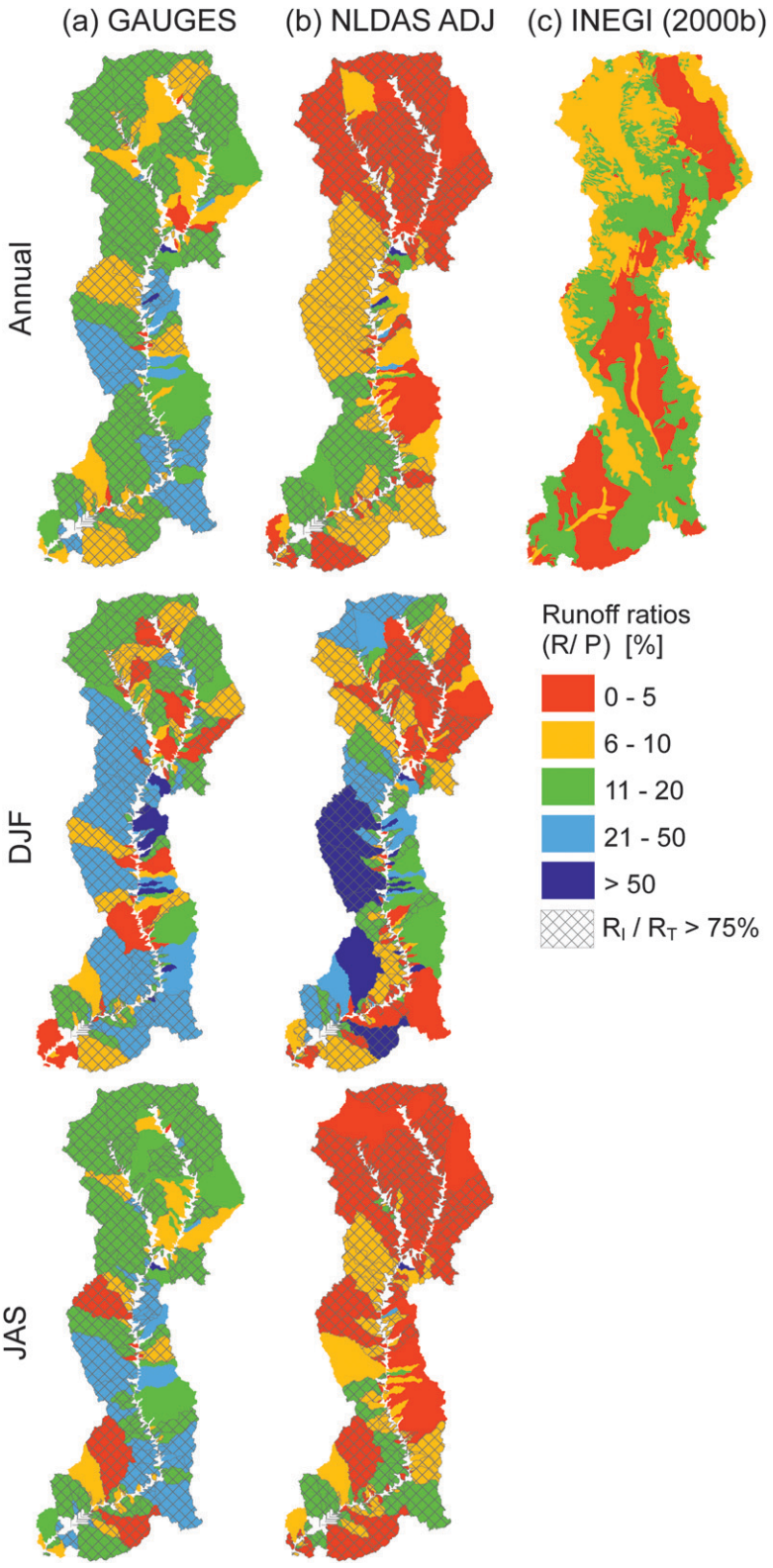

FIG. 14. Spatial variability of annual and seasonal runoff ratios (R/P) for (a) GAUGES and (b) NLDAS ADJ scenarios. (top) Annual, (middle) winter (DJF), and (bottom) summer (JAS) R/P. Subbasins with annual or seasonal $R_I/R_T > 75\%$ are hatched in all maps. (c) Annual runoff estimates from INEGI (2000b) are shown for comparison purposes.

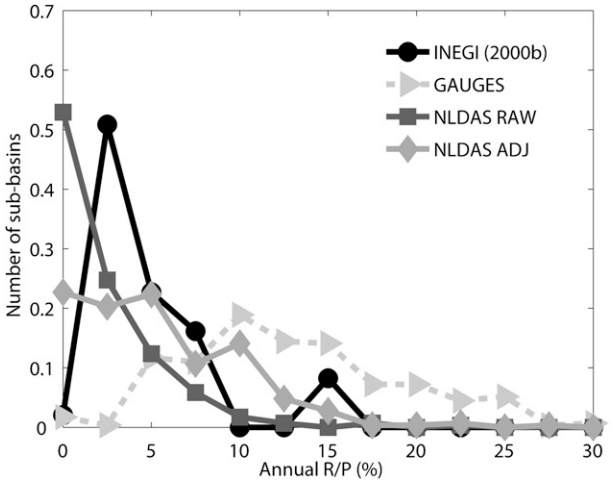

FIG. 15. Frequency distribution of the annual runoff ratio, R/P (%), for GAUGES, NLDAS ADJ, and INEGI (2000b) in the USR basin.

soil characteristics, whereas saturation-excess runoff and groundwater exfiltration were influenced by terrain features, which is consistent with field studies of Descroix et al. (2002a,b). NLDAS ADJ provided the most appealing spatial variations in precipitation and resulted in an annual runoff ratio that best matched an empirical estimate by INEGI (2000b) in terms of frequency and spatial distributions. As a result, the procedure for adjusting the NLDAS fields with ground data yielded large improvements in their utility for hydrologic applications, as suggested by Luo et al. (2003). An outcome of coupling the adjusted NLDAS forcing and distributed model is the production of a best available hydrologic prediction system that starts to meet the needs of water resources planners in the NAM region in terms of agreement with official estimates and in providing details at fine spatiotemporal scales.

The main goal of this study was to explore the relationship between evapotranspiration and the underlying runoff mechanisms. Through the distributed simulations in the large, heterogeneous watershed, we found a previously undocumented link between the mode of runoff generation and the evapotranspiration fluxes that mediate boundary layer processes. We identified that the fundamental relation between soil moisture and evapotranspiration exhibited large differences among subbasins characterized by different runoff mechanisms for the NAM period. Subbasins with large saturation-excess runoff and groundwater exfiltration contributions exhibit more ET because of the availability of deeper root zone soil moisture. The forms of the simulated ET–θ_S relations were also consistent with an observed relation obtained at an eddy covariance tower in the Sonora River (Vivoni et al. 2010). Furthermore, we identified that the production of evapotranspiration at annual and seasonal scales was related to the proportion of individual runoff components. An increase in ET occurred when the fraction of saturation-excess runoff increased in a subbasin, whereas an opposite trend was found for the proportion of infiltration-excess runoff. The simulations conducted in this study were conducted for a normal precipitation year. We expect that for wetter years, higher fractions of saturation-excess runoff and groundwater exfiltration would be observed, leading to ET rates that would be sustained for longer periods. During drier years, a higher proportion of infiltration-excess with minimal contributions of saturation-excess runoff and groundwater exfiltration are expected. These relations suggest that difficult-to-observe spatial differences in runoff mechanisms could potentially be inferred from more readily available estimates of the evapotranspiration field (e.g., Mu et al. 2007) or the ecosystem distributions that directly influence the atmospheric exchange (e.g., Tang et al. 2012). The link between runoff mechanisms and evapotranspiration also suggests that the coupling between water and energy processes in the heterogeneous land–atmosphere interface is more complex than previously thought in seasonally wet hydrologic systems.

Acknowledgments. This work was supported by the Mexican Council for Science and Technology through a fellowship to A.R-M. We also thank NOAA Climate Program Office (Grant GC07-019) and NSF IRES Program (Grant OISE 0553852) for support provided to conduct field activities. The following individuals contributed to the model setup, simulations, and data processing: Katelyn Watson, Rudiger Escobar, Giuseppe Mascaro, Luis A. Méndez-Barroso, Emily Van Dam, Cara Shonsey, and Richard Vendlinski. We also appreciate the datasets provided by CEA and CONAGUA.

REFERENCES

Acutis, M., and M. Donatelli, 2003: *SOIL*PAR 2.00: Software to estimate soil hydrological parameters and functions. *Eur. J. Agron.,* **18,** 373–377.

Arora, V. K., 2002: The use of the aridity index to assess climate change effect on annual runoff. *J. Hydrol.,* **265,** 164–177.

Batjes, N. H., 2002: Soil parameter estimates for the soil types of the world for use in global and regional modeling. International Food Policy Research Institute and International Soil Reference and Information Center Rep. 2002/02c, 52 pp.

Bedient, P. B., W. C. Huber, and B. E. Vieux, 2008: *Hydrology and Floodplain Analysis*. Prentice Hall, 816 pp.

Beven, K. J., and M. J. Kirkby, 1979: A physically-based variable contributing area model of basin hydrology. *Hydrol. Sci. Bull.,* **24,** 43–69.

Brito-Castillo, L., A. V. Douglas, A. Leyva-Contreras, and D. Lluch-Belda, 2003: The effect of large-scale circulation on precipitation and streamflow in the Gulf of California continental watershed. *Int. J. Climatol.,* **23,** 751–768.

Brown, D. E., 1994: *Biotic Communities of the Southwestern United States and Northwestern Mexico*. The University of Utah Press, 342 pp.

CEA, 2005: Estudio geo-hidrológico de las subcuencas de las Ríos Sonora, Zanjón, San Miguel, Mesa del Seri-La Victoria y cuenca Bacoachi. Comision Estatal del Agua Rep. CEA-ED-081 and CEA-ED-081-CA1, 391 pp.

Coblentz, D. D., and K. H. Riitters, 2004: Topographic controls on the regional-scale biodiversity of the southwestern USA. *J. Biogeogr.,* **31,** 1125–1138.

Cosgrove, B. A., and Coauthors, 2003: Real-time and retrospective forcing in the North American Land Data Assimilation System (NLDAS) project. *J. Geophys. Res.,* **108,** 8842, doi:10.1029/2002JD003118.

Daly, C., R. P. Neilson, and D. L. Phillips, 1994: A statistical-topographic model for mapping climatological precipitation over mountainous terrain. *J. Appl. Meteor.,* **33,** 140–158.

Descroix, L., J. L. Gonzalez-Barrios, D. Vandervaere, D. Viramontes, and A. Bollery, 2002a: An experimental analysis of hydrodynamic behaviour on soils and hillslopes in a subtropical mountain environment (Western Sierra Madre, Mexico). *J. Hydrol.,* **266,** 1–14.

——, J.-F. Nouvelot, and M. Vauclin, 2002b: Evaluation of an antecedent precipitation index to model runoff yield in the western Sierra Madre (North-west Mexico). *J. Hydrol.,* **263,** 114–130.

——, D. Viramontes, J. Estrada, J. L. Gonzalez Barrios, and J. Asseline, 2007: Investigating the spatial and temporal boundaries of Hortonian and Hewlettian runoff in Northern Mexico. *J. Hydrol.,* **346,** 144–158.

Dominguez, F., P. Kumar, and E. R. Vivoni, 2008: Precipitation recycling variability and ecoclimatological stability—A study using NARR data. Part II: North American monsoon region. *J. Climate,* **21,** 5187–5203.

Douglas, M. W., R. A. Maddox, K. Howard, and S. Reyes, 1993: The Mexican monsoon. *J. Climate,* **6,** 1665–1677.

Eltahir, E. A. B., 1998: A soil moisture–rainfall feedback mechanism: 1. Theory and observations. *Water Resour. Res.,* **34,** 765–776.

FAO, 1988: FAO-UNESCO soil map of the world: Revised legend. World Soil Resources Tech. Paper 20, 140 pp.

Forzieri, G., F. Castelli, and E. R. Vivoni, 2011: Vegetation dynamics within the North American monsoon region. *J. Climate,* **24,** 1763–1783.

García-Oliva, F., J. M. Maass, and L. Galicia, 1995: Rainstorm analysis and rainfall erosivity of a seasonal tropical region with a strong cyclonic influence on the Pacific coast of Mexico. *J. Appl. Meteor.,* **34,** 2491–2498.

Gebremichael, M., E. R. Vivoni, C. J. Watts, and J. C. Rodriguez, 2007: Submesoscale spatiotemporal variability of North American monsoon rainfall over complex terrain. *J. Climate,* **20,** 1751–1773.

Gochis, D. J., L. Brito-Castillo, and W. J. Shuttleworth, 2006: Hydroclimatology of the North American Monsoon region in northwest Mexico. *J. Hydrol.,* **316,** 53–70.

——, C. J. Watts, J. Garatuza-Payan, and J. Cesar-Rodriguez, 2007: Spatial and temporal patterns of precipitation intensity as observed by the NAME Event Rain gauge Network from 2002 to 2004. *J. Climate,* **20,** 1734–1750.

Goodrich, D. C., L. J. Lane, R. M. Shillito, S. N. Miller, K. H. Syed, and D. A. Woolhiser, 1997: Linearity of basin response as a function of scale in a semiarid watershed. *Water Resour. Res.,* **33,** 2951–2965.

Gutiérrez, J., and I. I. Hernandez, 1996: Runoff and interill erosion as affected by grass cover in a semi-arid rangeland of northern Mexico. *J. Arid Environ.,* **34,** 287–295.

Hallack-Alegria, M., and D. W. Watkins, 2007: Annual and warm season drought intensity–duration–frequency analysis for Sonora, Mexico. *J. Climate,* **20,** 1897–1909.

Hamlet, A. F., P. W. Mote, M. P. Clark, and D. P. Lettenmaier, 2007: Twentieth-century trends in runoff, evapotranspiration, and soil moisture in the western United States. *J. Climate,* **20,** 1468–1486.

Higgins, R. W., W. Shi, E. Yarosh, and R. Joyce, 2000: Improved United States precipitation quality control system and analysis. NCEP/Climate Prediction Center ATLAS 7, 40 pp.

INEGI, 2000a: Síntesis de información geográfica del Estado de Sonora. Instituto Nacional de Estadisticas y Geografia Rep., 88 pp.

——, 2000b: Cartas hidrologicas de aguas superficiales. Instituto Nacional de Estadisticas y Geografia Rep., 1 pp.

INEGI–INIFAP, 2001: Inventario nacional de suelos. Mexico Instituto Nacional de Estadisticas y Geografia and Instituto Nacional de Investigaciones Forestales, Agricolas, y Pecuarias Rep., 1 pp.

Ivanov, V. Y., E. R. Vivoni, R. L. Bras, and D. Entekhabi, 2004: Catchment hydrologic response with a fully distributed triangulated irregular network model. *Water Resour. Res.,* **40,** W11102, doi:10.1029/2004WR003218.

Joyce, R. J., J. E. Janowiak, P. A. Arkin, and P. Xie, 2004: CMORPH: A method that produces global precipitation estimates from passive microwave and infrared data at high spatial and temporal resolution. *J. Hydrometeor.,* **5,** 487–503.

Koster, R. D., and M. J. Suarez, 1999: A simple framework for examining the interannual variability of land surface moisture fluxes. *J. Climate,* **12,** 1911–1917.

Luo, L., and Coauthors, 2003: Validation of the North American Land Data Assimilation System (NLDAS) retrospective forcing over the southern Great Plains. *J. Geophys. Res.,* **108,** 8843, doi:10.1029/2002JD003246.

Luo, Y., E. H. Berbery, K. E. Mitchel, and A. K. Betts, 2007: Relationships between land surface and near-surface atmospheric variables in the NCEP North American Regional Reanalysis. *J. Hydrometeor.,* **8,** 1184–1183.

Mascaro, G., and E. R. Vivoni, 2010: Statistical and scaling properties of remotely sensed soil moisture in two contrasting domains in the North American monsoon region. *J. Arid Environ.,* **74,** 572–578.

Méndez-Barroso, L. A., and E. R. Vivoni, 2010: Observed shifts in land surface conditions during the North American Monsoon: Implications for a vegetation–rainfall feedback mechanism. *J. Arid Environ.,* **74,** 549–555.

Mitchell, K. E., and Coauthors, 2004: The multi-institution North American Land Data Assimilation System (NLDAS): Utilizing multiple GCIP products and partners in a continental distributed hydrological modeling system. *J. Geophys. Res.,* **109,** D07S90, doi:10.1029/2003JD003823.

Mora, F., and L. R. Iverson, 1998: On the sources of vegetation activity variation, and their relation with water balance in Mexico. *Int. J. Remote Sens.,* **19,** 1843–1871.

Mu, Q., F. A. Heinsch, M. Zhao, and S. M. Running, 2007: Development of a global evapotranspiration algorithm based on MODIS and global meteorology data. *Remote Sens. Environ.,* **111,** 519–536.

Muñoz-Arriola, F., R. Avissar, C. Zhu, and D. P. Lettenmaier, 2009: Sensitivity of the water resources of Rio Yaqui Basin, Mexico, to agriculture extensification under multiscale climate conditions. *Water Resour. Res.,* **45,** W00A20, doi:10.1029/2007WR006783.

Nesbitt, S. W., D. J. Gochis, and T. J. Lang, 2008: The diurnal cycle of clouds and precipitation along the Sierra Madre Occidental observed during NAME-2004: Implications for warm season precipitation estimation in complex terrain. *J. Hydrometeor.,* **9,** 728–743.

Paredes-Aguilar, R., T. Van Devender, and R. S. Felger, 2000: *Cactaceas de Sonora, Mexico: Su Diversidad, Uso y Conservacion*. IMADES Arizona-Sonora Desert Museum Press, 143 pp.

Pinker, R. T., and Coauthors, 2003: Surface radiation budgets in support of the GEWEX Continental-Scale International Project (GCIP) and the GEWEX Americas Prediction Project (GAPP), including the North American Land Data Assimilation System (NLDAS) project. *J. Geophys. Res.,* **108,** 8844, doi:10.1029/2002JD003301.

Robles-Morua, A., A. S. Mayer, M. T. Auer, and E. R. Vivoni, 2012: Modeling riverine pathogen fate and transport in Mexican rural communities and associated public health implications. *J. Environ. Manage.,* in press.

Rodríguez-Iturbe, I., and A. Porporato, 2004: *Ecohydrology of Water-Controlled Ecosystems*. Cambridge University Press, 442 pp.

Sankarasubramanian, A., and R. M. Vogel, 2002: Annual hydroclimatology of the United States. *Water Resour. Res.,* **38,** 1083, doi:10.1029/2001WR000619.

Schapp, M. G., F. J. Leij, and M. T. van Genuchten, 2001: Rosetta: A computer program for estimating soil hydraulic parameters with hierarchical pedotransfer functions. *J. Hydrol.,* **251,** 163–176.

Serrat-Capdevila, A., J. B. Valdes, J. G. Perez, K. Baird, L. J. Mata, and T. Maddock, 2007: Modeling climate change impacts—and uncertainty—on the hydrology of a riparian system: The San Pedro Basin (Arizona/Sonora). *J. Hydrol.,* **347,** 48–66.

Small, E. E., 2001: The influence of soil moisture anomalies on variability of the North American Monsoon System. *Geophys. Res. Lett.,* **28,** 139–142.

Smith, M. B., D.-J. Seo, V. I. Koren, S. M. Reed, Z. Zhang, Q. Duan, F. Moreda, and S. Cong, 2004: The Distributed Model Intercomparison Project (DMIP): Motivation and experiment design. *J. Hydrology,* **298,** 4–26.

Steiner, M., J. A. Smith, S. J. Burges, C. V. Alonso, and R. W. Darden, 1999: Effects of bias adjustment and rain gauge data quality control on radar rainfall. *Water Resour. Res.,* **35,** 2487–2503.

Tang, Q., E. R. Vivoni, F. Muñoz-Arriola, and D. P. Lettenmaier, 2012: Predictability of evapotranspiration patterns using remotely sensed vegetation dynamics during the North American monsoon. *J. Hydrometeor.,* **13,** 103–121.

Viramontes, D., and L. Descroix, 2003: Changes in the surface water hydrologic characteristics of an endoreic basin of northern Mexico from 1970 to 1998. *Hydrol. Processes,* **17,** 1291–1306.

Vivoni, E. R., V. Y. Ivanov, R. L. Bras, and D. Entekhabi, 2004: Generation of triangulated irregular networks based on hydrological similarity. *J. Hydrol. Eng.,* **9,** 288–302.

——, ——, ——, and ——, 2005: On the effects of triangulated terrain resolution on distributed hydrologic models. *Hydrol. Processes,* **19,** 2101–2122.

——, D. Entekhabi, R. L. Bras, and V. Y. Ivanov, 2007a: Control on runoff generation and scale-dependence in a distributed hydrologic model. *Hydrol. Earth Syst. Sci.,* **11,** 1683–1701.

——, H. A. Gutiérrez-Jurado, C. A. Aragon, L. A. Méndez-Barroso, A. J. Rinehart, and R. L. Wyckoff, 2007b: Variation of hydrometeorological conditions along a topographic transect in northwestern Mexico during the North American monsoon. *J. Climate,* **20,** 1792–1809.

——, H. A. Moreno, G. Mascaro, J. C. Rodríguez, C. J. Watts, J. Garatuza-Payan, and R. L. Scott, 2008: Observed relation between evapotranspiration and soil moisture in the North American monsoon region. *Geophys. Res. Lett.,* **35,** L22403, doi:10.1029/2008GL036001.

——, K. Tai, and D. J. Gohis, 2009: Effects of the initial soil moisture on rainfall generation and subsequent hydrologic response during the North American monsoon. *J. Hydrometeor.,* **10,** 644–664.

——, J. C. Rodríguez, and C. J. Watts, 2010: On the spatiotemporal variability of soil moisture and evapotranspiration in a mountainous basin within the North American monsoon region. *Water Resour. Res.,* **46,** W02509, doi:10.1029/2009WR008240.

——, G. Mascaro, S. Mniszewski, P. Fasel, E. P. Springer, V. Y. Ivanov, and R. L. Bras, 2011: Real-world hydrologic assessment of a fully-distributed hydrological model in a parallel computing environment. *J. Hydrol.,* **409,** 483–496.

Wood, E. F., and Coauthors, 2011: Hyperresolution global land surface modeling: Meeting a grand challenge for monitoring Earth's terrestrial water. *Water Resour. Res.,* **47,** W05301, doi:10.1029/2010WR010090.

Xu, J. J., W. J. Shuttleworth, X. Gao, S. Sorooshian, and E. E. Small, 2004: Soil moisture–precipitation feedback on the North American monsoon system in the MM5-OSU model. *Quart. J. Roy. Meteor. Soc.,* **130,** 2873–2890.